Article

Structure

Contactin 2 homophilic adhesion structure and conformational plasticity

Graphical abstract

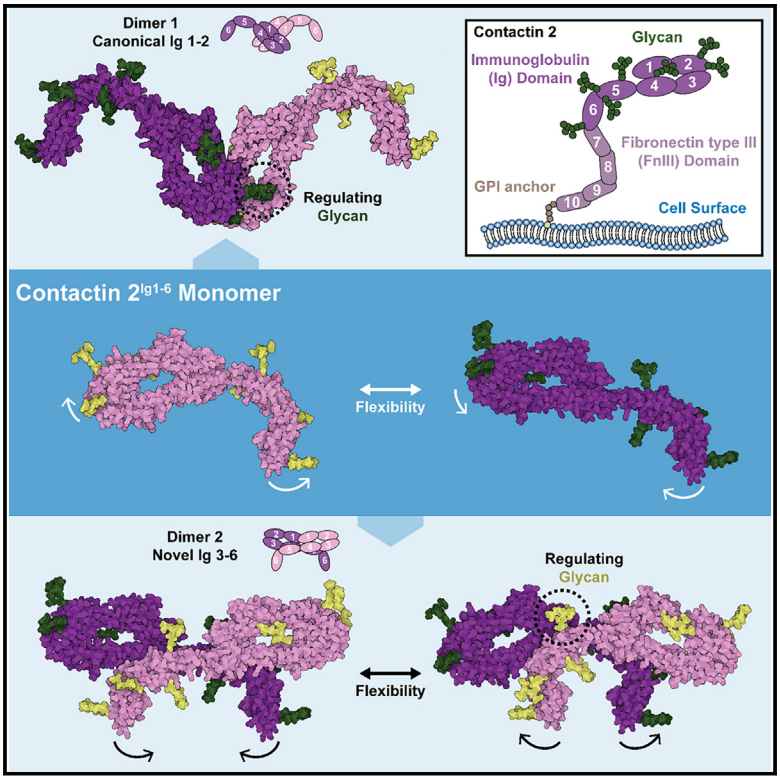

Highlights

- Contactin 2 structures have interdomain flexibility
- Contactin 2 Ig1-6 forms two distinct dimers that are Ig1-2 and Ig3-6 mediated
- Dimerization is glycan and glycan type dependent
- The interactions and structural plasticity explain contactin 2 mediated cell adhesion

Authors

Lucas M.P. Chataigner,
Lena Thärichen,
J. Wouter Beugelink, ..., Joost Snijder,
Friedrich Förster, Bert J.C. Janssen

Correspondence

b.j.c.janssen@uu.nl

In brief

Contactin 2 is a cell adhesion and signaling protein of the nervous system. Chataigner et al. show contactin 2 has structural flexibility and can form two different, glycan regulated dimers and larger oligomers. The structural data explain the adhesion role of contactin 2 in diverse cellular settings.

Chataigner et al., 2024, Structure *32*, 60–73
January 4, 2024
https://doi.org/10.1016/j.str.2023.10.012

CellPress

CellPress

Structure

Article

Contactin 2 homophilic adhesion structure and conformational plasticity

Lucas M.P. Chataigner,[1] Lena Thärichen,[1] J. Wouter Beugelink,[1] Joke C.M. Granneman,[1] Nadia J. Mokiem,[2] Joost Snijder,[2] Friedrich Förster,[1] and Bert J.C. Janssen[1,3,*]

[1]Structural Biochemistry, Bijvoet Centre for Biomolecular Research, Faculty of Science, Utrecht University, Universiteitsweg 99, Utrecht 3584 CG, the Netherlands

[2]Biomolecular Mass Spectrometry and Proteomics, Bijvoet Center for Biomolecular Research and Utrecht Institute of Pharmaceutical Sciences, Utrecht University, Padualaan 8, Utrecht 3584 CH, the Netherlands

[3]Lead contact

*Correspondence: b.j.c.janssen@uu.nl

https://doi.org/10.1016/j.str.2023.10.012

SUMMARY

The cell-surface attached glycoprotein contactin 2 is ubiquitously expressed in the nervous system and mediates homotypic cell-cell interactions to organize cell guidance, differentiation, and adhesion. Contactin 2 consists of six Ig and four fibronectin type III domains (FnIII) of which the first four Ig domains form a horseshoe structure important for homodimerization and oligomerization. Here we report the crystal structure of the six-domain contactin 2^{Ig1-6} and show that the Ig5-Ig6 combination is oriented away from the horseshoe with flexion in interdomain connections. Two distinct dimer states, through Ig1-Ig2 and Ig3-Ig6 interactions, together allow formation of larger oligomers. Combined size exclusion chromatography with multiangle light scattering (SEC-MALS), small-angle X-ray scattering (SAXS) and native MS analysis indicates contactin 2^{Ig1-6} oligomerizes in a glycan dependent manner. SAXS and negative-stain electron microscopy reveals inherent plasticity of the contactin 2 full-ectodomain. The combination of intermolecular binding sites and ectodomain plasticity explains how contactin 2 can function as a homotypic adhesion molecule in diverse intercellular environments.

INTRODUCTION

Contactin 2 (TAG-1/SNAP in rodent, and axonin-1/SC2 in chicken) is a cell surface molecule belonging to the contactin subfamily of the immunoglobulin-like cell adhesion molecule (IgCAM) family.[1] The contactin subfamily consist of a set of six related glycophosphatidylinositol (GPI)-membrane anchored proteins with six N-terminal immunoglobulin-like domains (Ig), four fibronectin type III domains (FnIII) and posttranslational modifications, e.g., N-linked glycosylation at multiple sites.[2] Contactins are expressed as either membrane attached or cleaved soluble forms across various tissues with strongest expression in the nervous system.[3–5] Crystal structures of contactin partial segments revealed thus far that Ig1-4 domains form a characteristic horseshoe supramodule with versatile binding capacity,[6–10] that the Ig5-FnIII2 domains are arranged in an extended head-to-tail conformation and that the FnIII2-3 connection is bent.[10]

The ubiquitous expression of contactin 2 across diverse brain regions and developmental time points,[1,5,11] in either membrane bound[1] or soluble[12–17] forms, underpins its critical role in cellular processes in development and activity of the nervous system. Contactin 2 has well established roles in neuronal cell proliferation, differentiation, death, and migration[18–21]; neurite outgrowth, and growth cone regulation[22–24]; axon guidance, fasciculation, and regeneration[24–28]; and in specific subcellular structures such as synapses,[29,30] the axon initial segment (AIS),[22,31] and the myelinating juxtaparanodal region.[32–34]

Contactin 2 homophilic interactions contribute to a number of cellular functions. Expression of contactin 2 induces cellular aggregation in several heterologous systems through resulting *trans*-cellular interaction.[6,35–39] Furthermore, contactin 2 has a well-documented role in dorsal root ganglion cellular adhesion and neurite extension.[27,40–43] Here, segments of the protein show neurite outgrowth promoting activity for contactin 2 positive cells,[43] while further works suggest homophilic interactions anchor motor neuron cell bodies and may be responsible for axonal fasciculation observed in contactin 2 positive cells.[27] Homophilic interactions of contactin 2 further likely contribute to migration of cells in the developing hindbrain along axons,[44] juxtaparanode adhesion,[33] restriction of retinal dendrites to specific layers,[45] and polarization of cerebral cortex cells.[20]

Competing models have been proposed for contactin 2 homophilic interactions. On the one hand it has been reported that C-terminal FnIII domains and not N-terminal Ig domains aggregate cells through *trans* cellular homophilic interaction.[36] On the other hand mutation of the Ig2 FG loop segment appears to abolish contactin 2 induced cellular aggregation, indicating

a direct role for Ig2 in adhesion.[6] Reduced contactin 2 induced cellular aggregation by antibodies directed toward N-terminal or C-terminal segments, lead to a *cis*-assisted *trans*-binding model for contactin 2 adhesion.[39] Structures of chicken[6] and human[7] contactin 2^{Ig1-4}, have been used to propose alternate zipper and dimerization mechanisms for contactin 2 immunoglobulin induced homophilic adhesion, both involving the Ig2 FG loop.

A line of evidence suggests contactin 2 homophilic interactions regulate heterophilic interactions. Complexes with NgCAM promoting neurite extension have been detected as higher-order molecular weight complexes,[41] while intercellular contactin 2 mediated adhesion initiates ankyrin recruitment by L1.[37] Contactin 2 homophilic adhesion also appears necessary for CASPR *trans* interaction in juxtaparanode adhesion.[33] Furthermore, immunoglobulin domains which can induce *trans* homophilic adhesion, are also involved in binding of NgCAM,[46] NrCAM and L1,[43] Kv channels,[47] and CASPR2,[47–49] suggesting possible competition between homophilic and heterophilic binding and highlighting the relevance of homophilic interactions in the function of contactin 2.

Given the importance of contactin 2 homophilic interactions in mediating critical cellular functions in the nervous system,[20,27,33,44,45] at different developmental stages,[1,3,4] and competing structural hypothesis for immunoglobulin induced homophilic adhesion,[6,7] we sought to gain further insights into its mode of homophilic adhesion and potential factors regulating this process. To this end, we structurally characterized mouse contactin 2^{Ig1-6} produced with either mannose rich or complex glycans, and contactin 2^{fe} (full ectodomain) produced with complex glycans. A 3.7 Å structure of contactin 2^{Ig1-6} reveals an interaction mode similar to that reported for human contactin 2^{Ig1-4} through an Ig2 interface,[7] albeit with more extensive Ig2 CD loop interactions in an interaction reminiscent of reported L1 family interactions.[50] An additional, different dimer is present, mediated by Ig3-Ig6 interactions, which may be relevant to understanding the formation of previously suggested higher order assemblies.[39] In the glycosidase-treated sample, contactin 2^{Ig1-6} is still substantially glycosylated, with larger glycan trees buried in the horseshoe and near the second dimer's interface. Steric hindrance of the glycosidase enzyme possibly explains the lack of glycan removal at these sites. Using MALS, small-angle X-ray scattering (SAXS) and native MS we report contactin 2^{Ig1-6} oligomerization which appears partially modulated by the type of N-glycan modifications. Interface mutations and site-directed glycan deletions confirm glycan and glycan-type dependent dimerization of contactin 2^{Ig1-6}. SAXS and negative stain EM of contactin 2^{fe} with complex glycans reveals an intrinsically flexible protein. Modeling of contactin 2^{fe} using partial structures is consistent with negative stain EM data and reveals, by evolutionary analysis, the location of possible interaction sites appearing as a patchwork of non-overlapping conserved interfaces.

RESULTS

Contactin 2^{Ig1-6} crystal structure reveals a highly flexible molecule

To gain quantitative and structural insights into domain contributions to contactin 2 homophilic interactions, we determined the structure of contactin 2^{Ig1-6} from a crystal that diffracted to a maximum resolution of 3.7 Å (PDB: 8A0Y) (Figures 1A, 1B, and S1A; Table 1). In this structure, the first four Ig domains adopt a typical horseshoe conformation, while the Ig5-Ig6 combination orients, nearly in plane, away from the horseshoe. This arrangement gives the molecule a distinct revolver-like architecture, with Ig1-Ig4 representing the "cylinder and barrel" region, and Ig5-Ig6 the "handle" (Figures 1B and 1C).

The presence of three independent contactin 2^{Ig1-6} molecules in our dataset allows comparison of conformations (Figure 1D), revealing conformational flexibility of contactin 2^{Ig1-6}. This flexibility can be described by one major and two minor hinging motions. For the major motion, the Ig5-Ig6 segment hinges 45° off the Ig1-Ig4 horseshoe at the Ig4-Ig5 connection (Figure 1D). In the first minor motion, Ig6 hinges 9° off Ig5 at the Ig5-Ig6 connection (Figure S1B), exacerbating mobility of the Ig5-Ig6 "handle" in its orientation with respect to the Ig1-Ig4 horseshoe. In the second minor motion, the Ig2-Ig3 unit hinges 15° off domains Ig1 and Ig4, bending the plane of the Ig1-Ig4 horseshoe (Figure 1D). As previously reported,[7] the horseshoe bending motion captured in our dataset, is also present in structures published for chicken (PDB:1CS6)[6] and human (PDB:2OM5)[7] contactin 2^{Ig1-4} (Figure S1C). The apparent flexibility captured in the contactin 2^{Ig1-6} crystal structure is likely relevant to its solution state, as SAXS measurements reveal normalized Kratky plots with bimodal and untapered shapes for both high-mannose and complex-glycan contactin 2^{Ig1-6} (Figure 1G). Indeed, normalized Kratky plots with such shapes are expected for a multidomain protein containing flexible regions. Flexibility of contactin 2^{Ig1-6} appears as an intrinsic property of the molecule with potential to modulate adhesive and signaling interactions.

The Ig1-Ig4 horseshoe segment in the larger Ig1-Ig6 structure we report, resembles previously reported chicken (PDB:1CS6)[6] and human (PDB:2OM5)[7] contactin 2^{Ig1-4} crystal structures with Cα r.m.s.d. of 1.10 Å and 1.18 Å respectively for the most conformationally similar chains. Furthermore r.m.s.d. of domains aligned individually often drop below 1 Å indicating that higher deviations in supramodules are likely due to conformational freedom of the assembly. Similarly, the Ig5-Ig6 combination of contactin 2^{Ig1-6} has Cα r.m.s.d. of 3.97 Å to the homologous combination in mouse contactin $3^{Ig5-FnIII2}$ (PDB:5I99),[10] while individual Ig 5 and 6 domains have 0.75 Å and 1.17 Cα RMSD, respectively.

Contactin 2^{Ig1-6} has seven N-linked glycosylation sites

Contactin 2 ectodomain sequence has 13 potential N-glycosylation sites, with seven of these sites predicted in the contactin 2^{Ig1-6} segment (Figure 1A).[51] Presence of electron density for the first N-acetylglucosamine (GlcNAc) residue at all seven positions in contactin 2^{Ig1-6} confirms that these sites are glycosylated (Figures 1A, 1B, and S1C). Contactin 2 vertebrate orthologue sequence conservation analysis[52] further reveals that 4 of 13 N-X-T/S glycosylation motifs in the contactin 2 ectodomain are in the bin for residues showing highest degree of conservation across orthologues (Figure 1A).

While contactin 2^{Ig1-6} used for crystallization was enzymatically treated with Endo-H_f, to deglycosylate the sample to enhance the chance of obtaining crystals, two glycosylation sites in the molecule are unaffected by the process, possibly due to

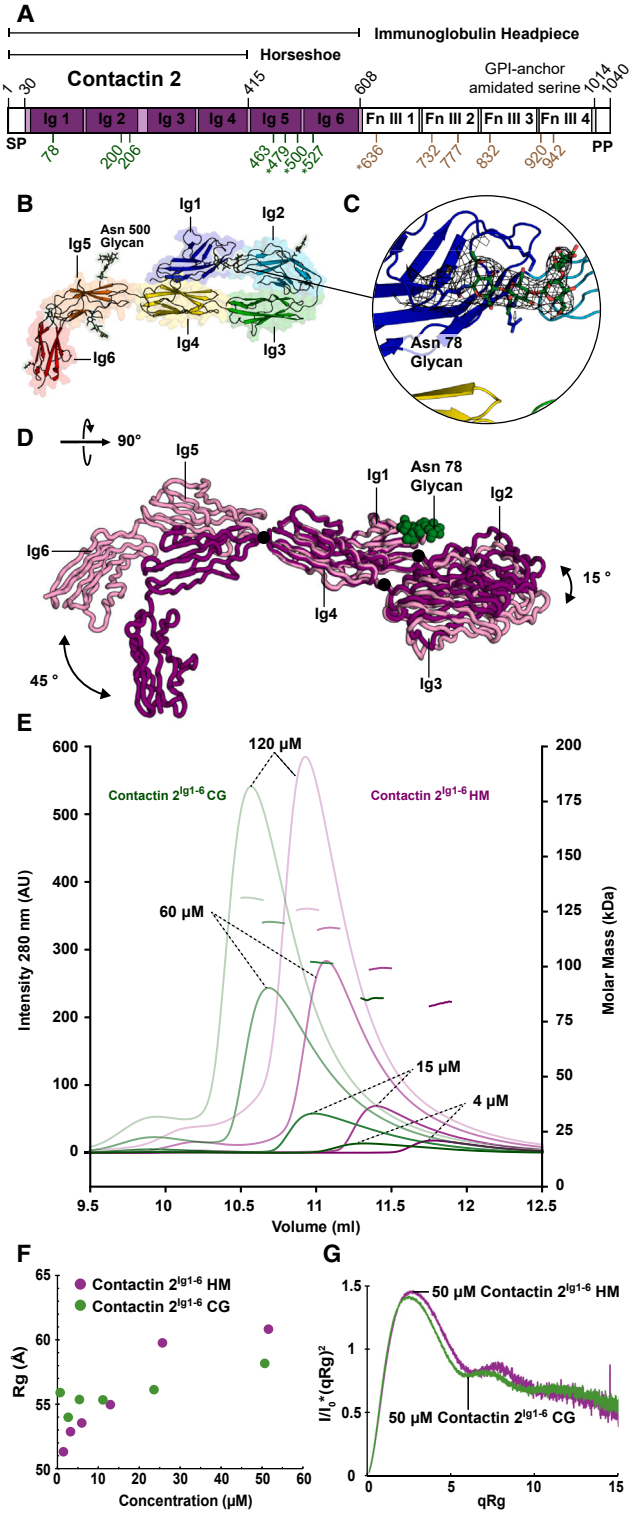

Figure 1. Structural and biophysical insights into contactin 2^{Ig1-6} flexibility, N-glycosylation and oligomerization

(A) Annotated sequence schematic of contactin 2. Immunoglobulin-like (Ig) and fibronectin type III (FnIII) domains are denoted with domain boundaries (top lines), and crystallized Ig segments colored in. N-glycosylation sites (bottom lines) confirmed by structures (green), predicted (brown), and highly conserved in orthologue conservation analysis (*). Signal peptide (SP), and pro-peptide (PP) are also indicated.

(B) Contactin 2^{Ig1-6} monomer (domain rainbow colored) with glycans shown as sticks and transparent spheres, displaying a revolver-like architecture.

(C) Asn 78 horseshoe buried glycan and associated density ($2mF_{obs}$-DF_{calc}) at 1σ.

(D) Superposed contactin 2^{Ig1-6} chains showing 45° Ig5-Ig6 hinging with respect to Ig4, and 15° Ig2-Ig3 hinging with respect to Ig1 and 4.

(E) Contactin 2^{Ig1-6} complex-glycan (CG) and high-mannose (HM) SEC-MALS analysis. Injection concentrations are indicated.

(F) Contactin 2^{Ig1-6} CG and HM batch SAXS analysis with Rg variations plotted by concentration.

(G) SAXS-based Kratky plots. The SEC-MALS and SAXS analysis reveal concentration-dependent dimerization and, possible higher-order oligomerization.

steric hindrance of the glycan moiety for the deglycosylation enzyme. For glycosylation sites at Asn 78 on Ig1 (Figures 1C and 1D), and Asn 500 on Ig4 (Figure S1A) sufficient electron density was consistently present to model the "stalk" of a high-mannose tree ($Man_1GlcNAc_2$) on all three contactin 2^{Ig1-6} chains present in the asymmetric unit. And in several cases an additional one to four mannoses (Man) could be modeled in the electron density at these two glycosylation sites. The presence of these more elongated glycosylation patterns suggests that the glycans at Asn 78 and Asn 500 remained sterically inaccessible to the Endo-H_f enzyme. For the glycan at Asn 78 this appears likely due to the intramolecular location of the site within the horseshoe (Figures 1C and 1D), while for the glycan at Asn 500 this is likely due to location near an intermolecular interface (Figure 2F). Mutation of the Asn 78 to an alanine in contactin 2^{Ig1-6}, thus preventing N-linked glycosylation at this site, resulted in substantially reduced secreted contactin $2^{Ig1-6\ N78A}$ whereas secretion of contactin $2^{Ig1-6\ N500A}$ was not affected (Figure 1D). This suggests a role for the glycan at Asn 78 in folding or stability of contactin 2, compatible with the observation of intramolecular interactions in the crystal structure.

Contactin 2^{Ig1-6} oligomerization appears partially dependent on N-glycan type

Peak shift and measured mass variation in size exclusion chromatography with multiangle light scattering (SEC-MALS) shows that contactin 2^{Ig1-6} dimerizes in solution in a concentration-dependent manner (Figure 1E, Table 2). The rate of assessed concentration-dependent dimerization of contactin 2^{Ig1-6} using this method appears independent on N-linked glycan type.

In agreement with the SEC-MALS analysis, batch SAXS experiments of contactin 2^{Ig1-6} at concentrations ranging from 1 to 52 µM reveal a concentration-dependent oligomerization. The high molecular weight (Mw) determined from I_0 indicates the presence of oligomers larger than contactin 2^{Ig1-6} dimers (Tables 3 and S1). The rates of oligomerization as assessed by increasing particle size at increasing concentration in SAXS analysis however show dependence on glycosylation type (Figures 1F and 1G) as material produced with more mannose like glycans (HM) oligomerizes more readily than material produced with more complex glycans (CGs). Also, in native mass spectrometry (native MS) analysis more dimers are present for contactin 2^{Ig1-6} containing high-mannose glycans compared to contactin 2^{Ig1-6} containing complex glycans and in both cases

a small fraction of oligomers larger than dimers is observed (Table 4, Figure S2).

Glycan modulated oligomerization of contactin 2^{Ig1-6} as reported here suggest that glycosylation sites near relevant interfaces with HM trees potentially favor oligomerization or that CG trees may sterically or electrostatically hinder it. Through structural analyses in the following sections and determining dimer formation of site-directed glycan deletions, we offer insights into structural features likely underlying the molecular details of this process.

Contactin 2^{Ig1-6} is present in two dimeric forms in the crystal

Analyses of intermolecular contacts in the contactin 2^{Ig1-6} crystal structure reveal presence of two dimeric contactin 2^{Ig1-6} arrangements, hereby referred to as the Ig1-2 dimer (Figure 2A) and Ig3-6 dimer (Figure 2B), that offer molecular insights into contactin 2^{Ig1-6} oligomerization. In the crystal structure, interfaces mediating these arrangements (Figures 2C and 2D) are occupied for all molecules, and are present in contacts formed between both asymmetric unit and symmetry related chains.

A few striking features stand out regarding these dimeric arrangements. On one hand both dimer interfaces bury extensive amounts of solvent accessible area ~1906 Å^2 (interface Ig1-2, Figure 2C) and ~3244 Å^2 (interface Ig3-6, Figure 2D). Furthermore, both interfaces show striking degrees of conservation in contactin 2 vertebrate orthologue sequence conservation analysis (Figures 2C and 2D). Lastly, both interfaces display potential for glycan-dependent modulation given proximity of glycosylation sites near these interfaces (Figures 2E and 2F). For glycosylation of Asn 200 on Ig2, one GlcNAc was originally modeled supported by density in our dataset owing to Endo-H_f treatment. However, modeling a full mannose tree ($Man_5GlcNAc_2$) at Asn 200 (Figure 2E) reveals how a more extended glycan presumably results in a glycan-glycan interface which may sterically constrain the formation of the Ig1-2 dimer (Figure 2A) depending on glycosylation microheterogeneity. As aforementioned, Asn 500 glycosylation appears sterically inaccessible to Endo-H_f treatment, and HM glycan trees ($Man_{3-5}GlcNAc_2$) could be modeled for this site in the electron density depending on the contactin 2^{Ig1-6} chain in the asymmetric unit. Glycosylation of Asn 500 on Ig4 could possibly impact formation of the Ig3-6 dimer (Figure 2F), as the HM glycan tree ends up in close proximity to the Ig1 in the other chain in the dimer. This intermolecular glycan-protein interface (Figure 2B) may stabilize potential Ig3-6 dimer formation.

To dissect the effects of glycosylation of Asn 200 and Asn 500 we introduced alanine mutations, preventing glycans to be added at these sites. Mutant contactin 2^{Ig1-6} proteins were produced with high-mannose or complex glycans at the remaining sequons and tested for dimer formation by native MS analysis. For contactin 2^{Ig1-6} high-mannose material, knockout of the glycan at Asn 200 does not affect dimerization, whereas knockout of the glycan at Asn 500 reduces dimerization (Table 4, Figure S2). This may indicate that a high-mannose glycan on Asn 500 aids in the dimerization via the Ig3-6 interface. For contactin 2^{Ig1-6} complex glycan material, however, both knockouts have elevated dimer levels compared to WT protein (Table 4, Figure S2). This suggests that complex-type glycans on both positions cause some steric hindrance or electrostatic repulsion for contactin 2 dimerization through the Ig1-2 and Ig3-6 interfaces and explain the slightly elevated dimer levels for contactin 2^{Ig1-6} with high-mannose glycans in SAXS and native MS (Figures 1F and S2; Table 4).

Table 1. Diffraction data collection and refinement statistics

	Cntn2^{Ig1-6}
Data Collection	
Space group	*C2*
Cell Dimensions	
a,b,c (Å)	131.9, 159.8, 227.9
α,β,γ (°)	90, 96.7, 90
Resolution (Å)	65–3.7 (3.82–3.70)[a]
Unique reflections	49878 (4525)
R_{merge}	0.150 (1.146)
I/σI	5.2 (0.9)
Completeness (%)	99.2 (98.1)
Redundancy	5.9 (6.1)
$CC_{1/2}$	0.975 (0.548)
Refinement	
Resolution (Å)	54.01–3.7
No. of reflections	49801
R_{work}/R_{free}	0.22/0.26
No. of atoms	
Protein	13275
Ligand/carb	615
Clashscore	6.64
B-factors (Å^2)	
Protein	229
Ligand/carb	262
TLS groups	18
R.m.s deviations	
Bond lenghts (Å)	0.002
Bond angles (°)	0.59
Ramachandran	
Favored (%)	93.4
Outliers (%)	0.3
Rotamer	
Outliers (%)	0.6
Molprobity Score	1.46
PDB ID	8A0Y

[a]Values in parentheses are for the highest resolution shell.

Similarities and differences in Ig1-2 mediated contactin 2 dimers

The 2-fold symmetric Ig1-2 mediated contactin 2^{Ig1-6} dimer interface presented here (Figures 2A, 2C, and 3A–3C) is reminiscent of the interaction modes reported for the neurofascin 186^{Ig1-4} homodimer,[50] the neurofascin 155^{Ig1-6} homodimer,[53] and the contactin 1^{Ig1-6} - neurofascin 155^{Ig1-6} complex.[53] In this dimer the Ig1-Ig4 horseshoes of contactin 2^{Ig1-6} interact in a near orthogonal edge-on orientation, largely using sides of the Ig2 domains

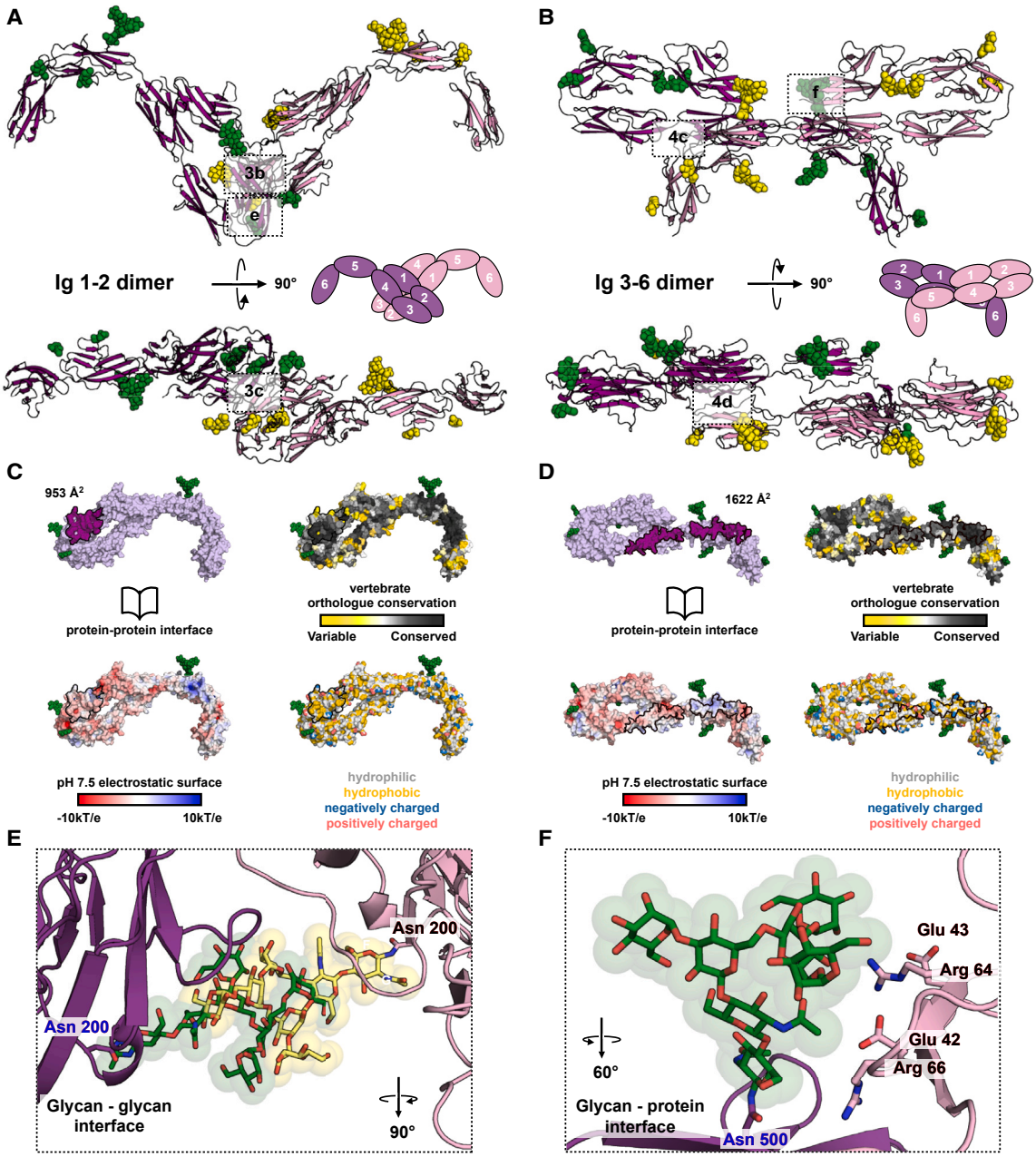

Figure 2. Contactin 2^{Ig1-6} has two dimer forms

(A) Cartoon representation of the contactin 2^{Ig1-6} Ig1-2 mediated dimer, with glycan residues (spheres), and a schematic indicating domain orientation.

(B) Same as in (A) for the contactin 2^{Ig1-6} Ig3-6 mediated dimer.

(C) Surface representation of contactin 2^{Ig1-6} with Ig1-2 mediated dimer interaction surface outlined and colored according to various properties. Relative conservation of the interface, suggesting a role in homophilic interactions.

(D) Same as in (C) for the contactin 2^{Ig1-6} Ig3-6 mediated dimer.

(E) 90° rotated view from (A) of Asn 200 glycan-glycan interface showing possible steric clashes of modeled glycans.

(F) 60° rotated view from (B) of Asn 500 glycan-protein interface showing potential for dimer stabilizing interactions.

for interaction with more modest Ig1 domain contributions (Figures 2A, 2C, and 3A–3C).

At the center of the Ig1-2 dimer interface presented here, a "super β sheet" is formed by joining of Ig2 GFC β-sheets of both molecules through antiparallel interaction of opposing G β-strands. At the "top side" of the "super β sheet", side chains of residues Lys 139 and Phe 223 of one chain, and Phe 217 and Thr 219 of the other chain form hydrophobic interactions that, due to the 2-fold nature of the dimer, are sandwiching the interface at both sides of the G strands (Figure 3A). Remarkably,

Table 2. Contactin 2^{Ig1-6} SEC-MALS data summary

Contactin 2^{Ig1-6}	Injection conc. (μM)	Peak conc. (μM)	Peak retention volume (mL)	MALS Mw (kDa)
High mannose Expected Mw monomer: 75.2 kDa	4	0.2	11.82	83.1 ± 2.5
	15	0.7	11.44	99.2 ± 0.8
	60	3	11.09	117.4 ± 0.2
	120	6	10.94	126.0 ± 0.4
Complex glycan Expected Mw monomer: 78.7 kDa	4	0.2	11.34	85.4 ± 2.6
	15	0.6	11.04	101.8 ± 0.4
	60	3	10.72	120.1 ± 0.1
	120	6	10.58	131.0 ± 0.3

Table 3. Contactin 2 batch small-angle X-ray scattering data summary

		Guinier			
Construct	Conc. (μM)	I_0	Mw from I_0 (kDa)	Rg (nm)	Oligomerization state
Contactin 2^{Ig1-6} High mannose Expected Mw monomer: 75.2 kDa	1	0.012	147	5.13 ± 0.87	2.0
	3	0.025	141	5.29 ± 0.63	1.9
	6	0.058	174	5.35 ± 0.23	2.3
	13	0.120	167	5.50 ± 0.14	2.2
	26	0.270	189	5.98 ± 0.15	2.5
	52	0.570	199	6.08 ± 0.10	2.6
Contactin 2^{Ig1-6} Complex glycan Expected Mw monomer: 78.7 kDa	1	0.014	146	5.59 ± 0.86	1.8
	3	0.030	203	5.40 ± 0.50	2.6
	5	0.055	186	5.54 ± 0.32	2.4
	11	0.120	193	5.53 ± 0.12	2.5
	24	0.250	191	5.61 ± 0.10	2.4
	51	0.600	213	5.82 ± 0.09	2.7
Contactin 2^{fe} Complex glycan Expected Mw monomer: 129.8 kDa	1	0.021	361	9.33 ± 3.04	2.8
	2	0.053	455	10.27 ± 1.62	3.5
	3	0.120	515	11.20 ± 1.05	4.0
	6	0.210	468	11.03 ± 0.64	3.6
	12	0.390	470	11.32 ± 0.66	3.6
	23	0.800	489	12.50 ± 0.64	3.8
	50	1.970	566	14.18 ± 0.72	4.4

See also Figure S6 and Table S1.

the Thr 219 residue kinks out disrupting the G strand beta sheet secondary structure enabling intermolecular hydrogen bonding with pseudo-A strand residue Glu 136 (Figure 3A). On the "bottom side" of the "super β-sheet", a concave half barrel forms that is closed off by the Ig2 CD loops and characterized by extensive hydrophobic contacts at its core involving side chains of Phe 175, Pro 176 and Phe 178 of both molecules in the dimer (Figure 3C). Overall, the interface is of a predominantly hydrophobic nature, with several hydrogen bonds possibly providing further stabilization (Figures 2A, 3B, and 3C).

Previous contactin 2^{Ig1-4} structures from chicken (PDB:1CS6)[6] and human (PDB:2OM5)[7] have offered competing Ig1-4 zipper and Ig1-2 dimer interaction modes (Figure S3A), both consistent with mutagenesis studies showing disrupted cell adhesion.[6] Our mouse contactin 2^{Ig1-6} Ig1-2 interaction is equally in accordance with previous mutagenesis studies showing disrupted cell adhesion,[6] as those targeted residues reside in the interface (Figure S3B).

Interestingly, while the mouse contactin 2^{Ig1-6} structure captures the same Ig1-2 interaction interface as human contactin 2^{Ig1-4} (PDB:2OM5),[7] the conformational arrangement and interaction mode differs between the two structures (Figures 3, S4A, and S4B). In the mouse structure, orthogonal horseshoes form a narrower X or cross shape (Figure 3A), given the less extensive beta strand secondary structure of the G strands (Figure 3B), which enables closer apposition of the hydrophobic residues in the CD loops forming a hydrophobic cocoon (Figure 3C). In the human structure the horseshoes form a flattened X shape (Figure 3D), as they are tilted by 33° more in plane, with more extensive antiparallel beta strand interactions supporting the interaction (Figure 3E). In the human contactin 2 structure, the hydrophobic cocoon does not form, as CD loops are positioned further away from one another (Figure 3F). This is exemplified by the 3.7 Å distance of the two Phe 178 sidechains in the dimer of mouse contactin 2^{Ig1-6} that are at a much larger distance of 14.2 Å in human contactin 2. Various factors may explain these different conformation-engaging residues in the interface in distinct ways. While the interface residues remain the same, differences in other regions—the human and mouse contactin 2 horseshoes have 94.3% sequence identity—may influence the homomeric interaction mode via the Ig1-2 interface. For example, the human and mouse contactin 2 have a different composition of the Ig2 FG turn and Ig1 AB loop, that may affect the Ig1-2 interface (Figures S4C and S4D). On the other hand, we cannot exclude that the different interaction modes may have arisen due to differences in crystal packing nor that they reflect structural plasticity of contactin 2 homodimer formation.

To assess the role of the Ig1-2 interface in mouse contactin 2 dimerization, we produced two variants by mutating residues in the hydrophobic cocoon to negative charged ones, contactin $2^{Ig1-6\ R169D,F175D,F178D,L210D}$ and contactin $2^{Ig1-6\ F175D,F178D}$, called interface 1a and 1b, respectively (Figure S1D). For contactin 2^{Ig1-6} complex glycan material, these mutants as compared to WT contactin 2^{Ig1-6} do not seem to affect dimerization. For contactin 2^{Ig1-6} high-mannose material, however, both mutants have reduced dimerization, with the largest effect for the more extensively altered interface, i.e., contactin $2^{Ig1-6\ R169D,F175D,F178D,L210D}$ (denoted interface 1a) (Table 4; Figure S2A). This indicates that, at least for the high-mannose version of contactin 2, the Ig1-2 interface plays a role in dimerization.

The contactin 2^{Ig1-6} Ig3-6 mediated dimer has conformational plasticity

The Ig3-6 mediated contactin 2^{Ig1-6} dimer interface presented here (Figures 2B, 2D, 2F, and 4A–4F) represents a potentially novel oligomerization interaction mode for contactin 2. This 2-fold symmetric Ig3-6 interface may have gone unreported previously as the contactin 2^{Ig1-6} crystal structure is the first detailed structure of contactin 2 that includes Ig5-6. In particular, the hinge areas at Ig3-Ig4 and Ig5-Ig6 are contacting each other in opposing molecules and form the core of the interaction interface, with looser contacts between sides of Ig4 and Ig5

Table 4. Contactin 2 dimer/monomer ratio from native MS

	Contactin 2^{Ig1-6}	Ratio dimer/monomer
High mannose	WT	1.64
	Interface1a	0.19
	Interface1b	0.46
	N200A	1.30
	N500A	0.42
Complex glycan	WT	0.57
	Interface1a	0.62
	Interface1b	0.51
	N200A	1.07
	N500A	1.31

See also Figure S2.

extending it, resulting in a butterfly shaped dimeric arrangement (Figure 2B).

The Ig3-6 interface buries a near continuous extended patch (Figure 2D). Mixed hydrophilic, complementary charged, and hydrophobic interactions are present at the Ig3-4 and Ig5-6 "hinges" portion of the interface. For example, Arg 508 from the Ig5-6 hinge forms a salt bridge with Glu 330 as it is maintained in place by a hydrogen bond with Ig5 Ser 506, while the Ig6 BC loop Thr 539 backbone hydrogen bonds with the backbone of Gly 354 in the Ig4-5 hinge (Figure 4C). These interactions seem to contribute to correct orientation of the Ig3-6 domains permitting more extensive hydrophobic contacts that sandwich the "hinge" portion. On the left side of the "hinge" interface, Ig3 Phe 300 interacts with Ig6 BC loop Pro 538 (Figure 4C), while on the right side a more extensive hydrophobic cluster is formed by hydrophobic residues from the Ig3 facing end of the Ig4 domain that are contacting hydrophobic residues located near the Ig5-Ig6 connection in the opposing molecule (Figure 4D). Loosely packed additional charged and hydrophilic interactions in the hinge interface and Ig4–5 segment additionally contribute to the interface. Overall, the Ig3-6 interface is of a mixed hydrophobic and hydrophilic nature, with striking electrostatic complementarity (Figure 2D). The Ig3-Ig6 dimer interface consists of two extended patches (Figure 2D) and we mutated residues in both patches to assess dimerization through this interface. Unfortunately, this mutant, Leu332Asp, Ala353Asp, Arg508Asp, and Met540Asp, denoted interface 2, was not secreted, preventing us from assessing the effect on dimerization (Figure S1D).

Two conformational arrangements of the Ig3-6 contactin 2^{Ig1-6} dimer are present in the crystal structure that accommodate the structural plasticity of the Ig4-5 and Ig5-6 connections (Figures 4A, 4B, and S5). The two Ig3-6 dimer states capture a complex motion that resembles the flapping of a butterfly's wings from a more "spread" to a more "strained" position which results in the dimer C-termini exchanging from a more distant 10 nm to a closer 5 nm apart position (Figures 4A and 4B). The core of the "hinges" dimer interface is conserved between the two dimer states, nonetheless looser charged and hydrophilic interactions occurring at the sides engage in distinct ways. In the "hinges" portion a number of changes occur. Lys 355 interacting with

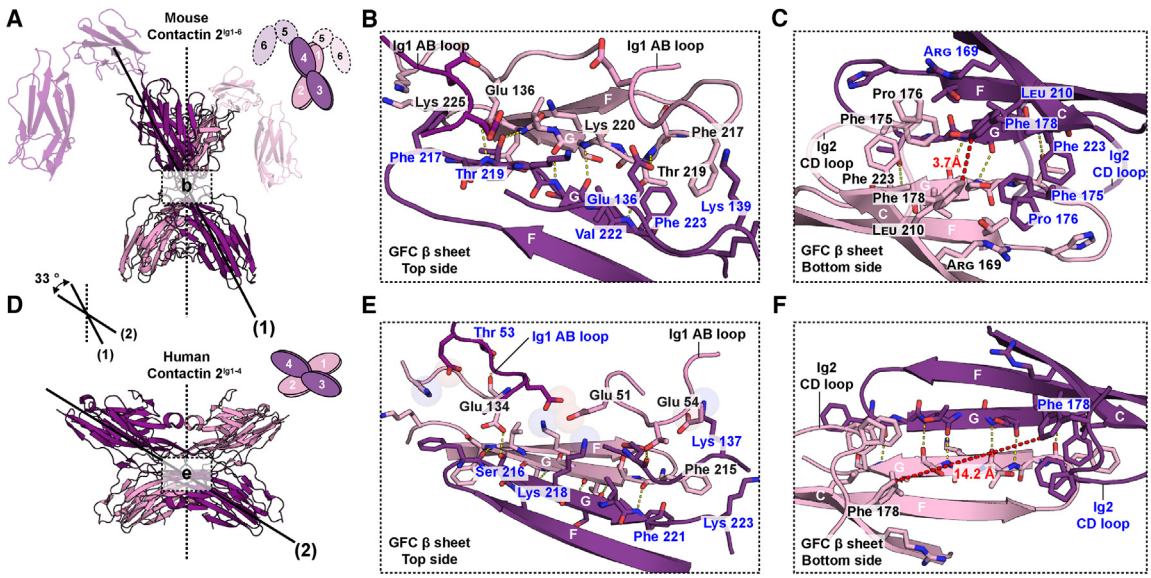

Figure 3. Similarities and differences between mouse and human contactin 2 Ig1-2 mediated dimers and Ig1-2 GFC super beta sheet interfaces

(A) Orthogonal horseshoes from mouse contactin 2^{Ig1-6} forming a narrower X shape and a schematic indicating domain orientation. The narrower X-shape leads to less extensive beta strand secondary structure of the G strands (B), which enables closer apposition of the hydrophobic residues in the CD loops forming a hydrophobic cocoon (C).

(D) Orthogonal horseshoes from human contactin 2^{Ig1-4} forming a broader X shape and a schematic indicating domain orientation. The broader X-shape results in more extensive beta strand secondary structure of the G strands (E) and in more distant positioning of CD loops preventing hydrophobic cocoon formation (F). The difference in distance, from 3.7 to 14.2 Å, between the Phe 178 sidechains is indicated by a dotted red line in (C) and (F). The dotted black lines in (A) and (D) indicate the 2-fold symmetry axis.

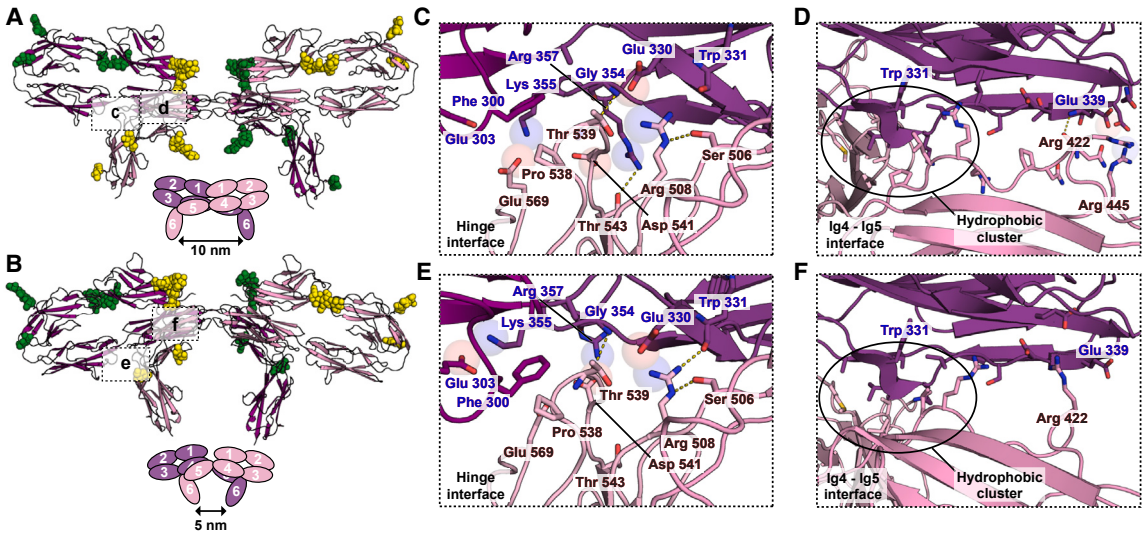

Figure 4. Conformational plasticity of contactin 2 Ig3-6 mediated dimer and effects on "hinge" and "Ig4-5" interface portions

(A) "Spread" conformation of Ig3-6 contactin 2 dimer resulting in more distant C-terminal Ig6 domains. Maintaining this configuration are extensive charged (C) and hydrophobic (D) residue interactions in the hinge region, and closer apposition of Ig4 and 5 domains (D).

(B) "Strained" conformation of Ig3-6 contactin 2 dimer resulting in closer C-terminal Ig6 domains. In this configuration several charged residues swap interactions in the hinge region (E), the hydrophobic hinge region cluster is predominantly maintained (F), while Ig4 and 5 domains more loosely contact each other (F).

Glu 569 (Figure 4C) swaps from an intermolecular interaction to an intramolecular interaction with Glu 303 (Figure 4E). Arg 357 forming a salt bridge with Asp 541 in both conformations loses a hydrogen bond with Thr 543 (Figures 4C and 4E), while Arg 508 gains a hydrogen bond to the Trp 331 backbone carbonyl oxygen (Figures 4C and 4E). The most striking changes however occur in the Ig4-Ig5 edge interactions which are mostly lost in the "strained" conformation (Figures 4D and 4F). Here, loss of Arg 422 backbone hydrogen bond to Glu 339, and Arg 445 salt bridge to Glu 339, results in loss of more extensive contacts between Ig4 and Ig5 and changes in Ig5 secondary structure elements comparing the "spread" conformation with the "strained" one.

Contactin 2^{fe} has structural plasticity and undergoes concentration-dependent oligomerization

To see if we could extrapolate insights gained by characterization of contactin $2^{Ig1\text{-}6}$ segment to behavior of the full-length molecule we further sought to structurally characterize contactin 2^{fe}. In this case, suitable contactin 2^{fe} material produced with high-mannose type glycans for biophysical characterization could not be obtained due to aggregation of the sample, we could however obtain stable sample with complex glycans by purifying contactin 2^{fe} in high salt and imidazole containing buffer (25 mM HEPES pH 7.5, 500 mM NaCl, 500 mM Imidazole). Given the intrinsic flexibility of contactin 2 established by our characterization of the contactin $2^{Ig1\text{-}6}$ segment we turned to low resolution techniques and in silico approaches to obtain structural insights into contactin 2^{fe} function.

Using SAXS measurements we establish that contactin 2^{fe} oligomerizes (Figure 5A), and, judged from the molecular weight, the oligomers may represent trimers or tetramers (Table 3; Figures S6A–S6C), or a mixture of different oligomeric species. Size-exclusion chromatography comparing contactin 2^{fe} and the paralog contactin 1^{fe} indicate contactin 2^{fe} elutes as an oligomer, whereas contactin 1^{fe} is a monomer (Figure S6D) as shown previously.[53] Kratky plots with bimodal and untapered shapes illustrate the contactin 2 ectodomain behaves as a multidomain protein containing flexible regions in solution (Figure 5B), even more so compared to contactin $2^{Ig1\text{-}6}$. The concentration-dependent oligomerization of contactin 2^{fe} in the SAXS experiments complicates the modeling of the data and hence we have not tried to fit an *ab initio* or rigid-body model.

To quantitatively assess the flexibility of contactin 2^{fe} we turned to negative stain electron microscopy. Here, micrographs revealed predominantly monodisperse molecules likely owing to the low concentration sample conditions, of 39 nM, required for imaging (Figure 5C). Additionally, in these images the horseshoe structure of the first four domains is strikingly apparent as molecules appear to sample a variety of linear, backfolded, and sinusoidal conformational arrangements that suggest intrinsic flexibility of the molecule (Figure 5C). 2D classification revealed several class averages representing distinct linear and U-shaped forms (Figure 5D). For a number of subclasses only few domain segments are resolved, consistent with potential hinging between domain-domain connections along contactin molecules as reported here in the Ig segment and by others in the FnIII segment.[10]

To validate insights gained from low-resolution negative-stain imaging, we built straightforward higher-resolution models for contactin 2^{fe} (Figures 5E, S7A, and S7B). These models were generated using crystal structures of conformationally distinct contactin $2^{Ig1\text{-}6}$ chains, mouse contactin $2^{FnIII1\text{-}3}$ (PDB:5EQ4),[10] and an AlpaFold[54] fourth FnIII domain model. These structures were superposed with contactin $3^{Ig5\text{–}FnIII2}$ (PDB:5I99)[10] to determine a sensible Ig6-FnIII1 orientation, and using the Alphafold Protein Structure Database (Alphafold PSD)[54,55] for a sensible FnIII3-4 connection. Calculated projections of one model

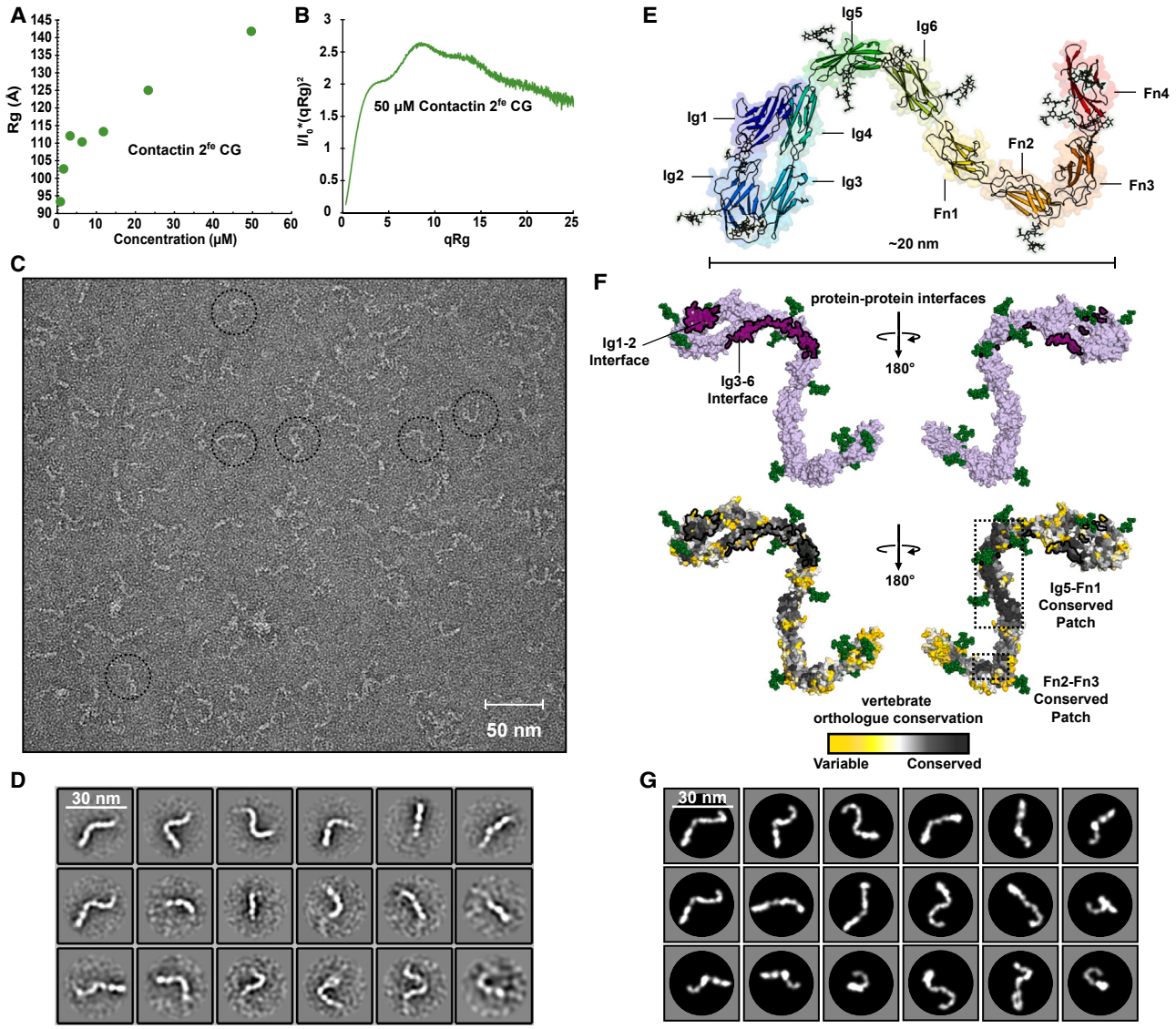

Figure 5. Concentration-dependent oligomerization and structural plasticity of contactin 2^{fe}

Contactin 2^{fe} batch SAXS analysis with Rg variations plotted by concentration (A) and characteristic normalized Kratky plot (B).

(C) Representative micrograph of negatively stained contactin 2^{fe} (at 39 nM), showing predominantly monodisperse particles, characteristic Ig1–4 horseshoe at one end of the molecules (examples highlighted by dashed circles), and broad conformational landscape suggesting inherent flexibility.

(D) Top eighteen 2D class averages of contactin 2^{fe} corresponding to 1637 particles.

(E) Model of contactin 2^{fe} generated by alignment and superposition of partial structures (see text).

(F) Vertebrate orthologue conservation analysis extended to the contactin 2^{fe} model showing a patchwork of conserved interfaces.

(G) Representative projections calculated from the contactin 2^{fe} model in (E), showing some similarity with the class averages in (D).

(Figures 5E–5G), provide 2D views of contactin 2 ectodomain that recapitulate observed features in negative-stain micrographs and the class averages (Figures 5C and 5D) albeit that in most class averages not all domains are visible, probably due to the structural heterogeneity arising from the hinging in domain-domain connections, and resultant blurring of density after averaging. Interestingly, projections derived from the crystal structure-based models appear to correspond better to the particle conformations observed by negative stain than the *in silico* Alphafold ectodomain model (Figure S7).

Given that both C-terminal and N-terminal contactin 2^{fe} regions have been implicated in various heterophilic and homophilic interactions, we decided to extend the conservation mapping to our ectodomain chain model (Figure 5F). In this model, 4 highly conserved "patches" stand out (Figure 5F). These include the two interfaces we capture in our crystal structure, that we speculate underlie oligomerization. As well as an extended surface from Ig5 to FnIII1 found on the "opposite" side of the Ig3-6 interface, and a patch on sides of FnIII2-FnIII3. Patches on Ig5 to FnIII1 and FnIII2-FnIII3 stand out as likely potentially

relevant to interactions given reports that the Ig5 to FnIII1 is the minimal required segment for contactin-CASPR2 interactions,[49] and that fibronectin domains help mediate contactin 2 homophilic interactions.[36,39] Remarkably, modeling ectodomain structures into dimer or trimer assemblies, using the contactin 2^{fe} models and crystal packing reported here, illustrates that various potential interactions do not obstruct one another (Figure S8) and, considering the presence of some flexion in domain connections, the models are compatible with *cis* or *trans* cellular interactions.

DISCUSSION

Similar to several other multi-domain subfamilies of the IgCAM family, such as DSCAM, sidekick and L1, contactin 2 is characterized by an N-terminal horseshoe and intrinsic conformational inter-domain flexibility.[53,56,57] The horseshoe is often involved in homophilic interactions, albeit using strikingly different faces of the module, and the members of these subfamilies differ substantially in number of domains.[58] Diversity in size and inherent structural plasticity explains the function of these proteins in defining adhesion specificity at different intermembrane environments in numerous tissues.

Contactin 2 itself has pleotropic functions. Through roles in diverse environments contactin 2 contributes to functional wiring of the nervous system.[1] Structural plasticity and intermolecular interaction of contactin 2 that we uncover here likely play important roles in enabling it to mediate adhesive and signaling interactions in different cellular contexts. On one hand, more elongated conformations may permit sensing of longer range cues outside neuronal cells that underlie some of its functions in cellular migration,[18–21] neurite outgrowth,[22–24] and axon growth and regeneration.[24–28] While on the other hand, the ability to fold into more compact arrangements, such as the Ig3-6 mediated dimer could underscore its functions at diverse cellular contact sites such as synapses,[29,30] the myelinating juxtaparanodal region,[32–34] and between fasciculated axons[27] which dynamically sample a diverse range of intercellular distances. Furthermore, by permitting presentation of protein interaction sites arranged in distinct topologies the wide conformational landscape of contactin 2 likely allows engagement with its structurally diverse reported protein partners including IgCAMs from contactin,[1,3,4] L1,[37,43] and NgCAM[41,46] protein families, but also CASPR2,[29,31,33,34,47–49] Kv1 ion channels,[47] amyloid precursor protein,[59] and tropomyosin receptor kinase B (TrkB).[28]

Expression of contactin 2 in heterologous systems induces cellular aggregation through resulting *trans*-cellular interaction,[6,35–39] and these *trans* interactions play a role in contactin 2 function in the biological setting exemplified by contactin 2 mediated adhesion to form and maintain axon-myelin interactions at the juxtaparanodal region.[32–34] Both chicken[6] and human[7] contactin $2^{Ig1\text{-}4}$ structures, have been used to propose alternate zipper and dimerization mechanisms for homophilic adhesion both involving an Ig2 FG loop, which when mutated abolishes cellular aggregation. The mouse crystallographic contactin $2^{Ig1\text{-}6}$ structure presented here, captures the same highly conserved Ig1-2 interface as human contactin $2^{Ig1\text{-}4}$ [7] and is equally in accordance with previous mutagenesis studies. Remarkably, while capturing the same interaction interface as the human structure, Ig1-2 engaged in dimer interaction in mouse contactin $2^{Ig1\text{-}6}$ presents a distinct conformational arrangement with more extensive hydrophobic contacts in the CD loops, enabling the formation of a hydrophobic cocoon reminiscent of dimer interaction modes proposed for L1 family members.[50] Ultimately, the distinct conformational arrangements that we identify, highlight the plasticity of contactin 2 and potentially enables looser or more constricted forms of engagement in a cellular context.

N-linked glycosylation patterns have previously been shown to regulate function of proteins from the contactin family. In particular glycosylation of contactin 1 modulates its interactions with paranodal adhesion partner neurofascin 155.[53,60–62] To date, N-linked glycosylation has however not been known to mediate a role in contactin 2 functionality. Through detailed biophysical characterization the work presented here illustrates that contactin $2^{Ig1\text{-}6}$ is a highly glycosylated segment of the molecule, that N-linked glycan type appears to partially modulate its oligomerization *in vitro*, and that glycosylation of Asn residues 200 and 500 are most likely candidates to directly explain this process through proximity to interaction sites showing high conservation. Dimerization analysis of glycan knockouts Asn200Ala and Asn500Ala support our notion that complex glycans at these sites hinder dimerization, possibly by steric hindrance or electrostatic repulsion from charged glycans, and that both the Ig1-2 and the Ig3-6 interfaces play a role in contactin 2 dimerization. Furthermore the glycan-type-dependent difference in dimerization of the Ig1-2 interface mutants, contactin $2^{Ig1\text{-}6\ R169D,F175D,F178D,L210D}$ and contactin $2^{Ig1\text{-}6\ F175D,F178D}$, suggest a role for glycans in modulating dimer formation. Determining if and how these interfaces and the glycans contribute to *cis* or *trans* cellular interactions will require future work. Finally, given the importance of Ig1-Ig2 interactions, an Ig1-Ig2 hinge, proximity of the Ig1 Asn 78 glycan tree to Ig2 and loss of secretion of contactin $2^{Ig1\text{-}6}$ Asn78Ala from HEK293 cells (Figure S1D), it appears likely the glycan tree composition at this site could play a role in protein stability or constraining molecular motion.

Several segments along the contactin 2 molecule have been shown to contribute to cellular aggregation through underlying homophilic interactions, resulting in the postulate that the molecule may form higher-order assemblies through combined interaction sites.[6,7,36,39] Resolving organization of the larger contactin $2^{Ig1\text{-}6}$ segment, we uncover the potential for the molecule to form higher-order oligomers through two complementary dimers using highly conserved Ig1-Ig2 and Ig3-Ig6 interfaces that do not obstruct one another in the full-length molecule (Figure S8). While further work will be needed to assess functional relevance of these interfaces in the biological setting, it is equally interesting that in the potential assemblies additional conserved patches in the full-length molecule remain unobstructed (Figures 5E and S8). This feature is noteworthy as additional patches stand out as segments previously reported to mediate CASPR2 interactions,[49] and fibronectin mediated homophilic interactions.[36,39]

Contactin 2 is a molecule whose study has been of long-standing interest given its ubiquitous roles in functionally wiring vertebrate tissues, and in particular the nervous system.[1,4,5] Molecular principles governing its biological action have remained poorly understood in face of limited structural information

regarding organization of larger segments, hampering potential breakthroughs in treating associated pathologies in cancer,[63,64] cardiac tissue malfunction,[65–67] learning and memory deficiency,[68–70] nervous system regeneration,[28,71–73] neurodevelopmental disorders,[74,75] and neurodegenerative diseases.[70,76–81] The structural and biophysical characterization of larger contactin 2 segments reported here provide a basis for further work to resolve the molecular mechanism underlying contactin 2 function in health and disease.

STAR★METHODS

Detailed methods are provided in the online version of this paper and include the following:

- KEY RESOURCES TABLE
- RESOURCE AVAILABILITY
  - Lead contact
  - Materials availability
  - Data and code availability
- EXPERIMENTAL MODEL AND STUDY PARTICIPANT DETAILS
  - Cell lines
  - Microbe strains
- METHOD DETAILS
  - Construct generation and mutagenesis
  - Protein expression and purification
  - Crystallization and X-ray data collection
  - Structure determination and refinement
  - Structural analyses
  - Small-angle X-ray scattering
  - SEC-MALS
  - Negative stain electron microscopy
  - Image processing for 2D classification
  - Native mass spectrometry
- QUANTIFICATION AND STATISTICAL ANALYSIS

SUPPLEMENTAL INFORMATION

Supplemental information can be found online at https://doi.org/10.1016/j.str.2023.10.012.

ACKNOWLEDGMENTS

We thank the staff of the DLS beamline I03 for help with X-ray diffraction data collection and DLS beamline B21 for help with SAXS data collection. This project has received funding from the European Research Council (ERC) under the European Union's Horizon 2020 research and innovation programme with grant agreement No. 677500 (to B.J.C.J.).

AUTHOR CONTRIBUTIONS

B.J.C.J conceived the project. L.M.P.C designed experiments with input from B.J.C.J. B.J.C.J and J.C.M.G cloned constructs. L.M.P.C purified recombinant proteins and performed structural and biophysical experiments (X-ray diffraction and SAXS). J.W.B purified mutant proteins and performed SEC-MALS experiments. L.M.P.C processed various data (SEC-MALS, X-ray diffraction, and SAXS) L.T performed negative stain electron microscopy experiments and data analysis under supervision of F.F. N.J.M performed native mass spectrometry experiments and data analysis under supervision of J.S. L.M.P.C analyzed the structural information. B.J.C.J supervised the project. L.M.P.C and B.J.C.J and wrote the manuscript. All authors commented on the manuscript.

DECLARATION OF INTERESTS

The authors declare no competing interests.

Received: June 21, 2022
Revised: September 27, 2023
Accepted: October 26, 2023
Published: November 21, 2023

REFERENCES

1. Masuda, T. (2017). Contactin-2/TAG-1, active on the front line for three decades. Cell Adh. Migr. *11*, 524–531. https://doi.org/10.1080/19336918.2016.1269998.
2. Mohebiany, A.N., Harroch, S., and Bouyain, S. (2014). New insights into the roles of the contactin cell adhesion molecules in neural development. Adv. Neurobiol. *8*, 165–194.
3. Shimoda, Y., and Watanabe, K. (2009). Contactins: emerging key roles in the development and function of the nervous system. Cell Adh. Migr. *3*, 64–70.
4. Chatterjee, M., Schild, D., and Teunissen, C.E. (2019). Contactins in the central nervous system: role in health and disease. Neural Regen. Res. *14*, 206–216. https://doi.org/10.4103/1673-5374.244776.
5. Morris, J., Leung, S.S.Y., Bailey, M.E.S., Cullen, B., Ferguson, A., Graham, N., Johnston, K.J.A., Lyall, D.M., Lyall, L.M., Ward, J., et al. (2020). Exploring the Role of Contactins across Psychological, Psychiatric and Cardiometabolic Traits within UK Biobank. Genes *11*, 1326. https://doi.org/10.3390/genes11111326.
6. Freigang, J., Proba, K., Leder, L., Diederichs, K., Sonderegger, P., and Welte, W. (2000). The crystal structure of the ligand binding module of axonin-1/TAG-1 suggests a zipper mechanism for neural cell adhesion. Cell *101*, 425–433.
7. Mörtl, M., Sonderegger, P., Diederichs, K., and Welte, W. (2007). The crystal structure of the ligand-binding module of human TAG-1 suggests a new mode of homophilic interaction. Protein Sci. *16*, 2174–2183. https://doi.org/10.1110/ps.072802707.
8. Bouyain, S., and Watkins, D.J. (2010). The protein tyrosine phosphatases PTPRZ and PTPRG bind to distinct members of the contactin family of neural recognition molecules. Proc. Natl. Acad. Sci. USA *107*, 2443–2448. https://doi.org/10.1073/pnas.0911235107.
9. Lamprianou, S., Chatzopoulou, E., Thomas, J.L., Bouyain, S., and Harroch, S. (2011). A complex between contactin-1 and the protein tyrosine phosphatase PTPRZ controls the development of oligodendrocyte precursor cells. Proc. Natl. Acad. Sci. USA *108*, 17498–17503. https://doi.org/10.1073/pnas.1108774108.
10. Nikolaienko, R.M., Hammel, M., Dubreuil, V., Zalmai, R., Hall, D.R., Mehzabeen, N., Karuppan, S.J., Harroch, S., Stella, S.L., and Bouyain, S. (2016). Structural Basis for Interactions Between Contactin Family Members and Protein Tyrosine Phosphatase Receptor Type G in Neural Tissues. J. Biol. Chem. *291*, 21335–21349. https://doi.org/10.1074/jbc.M116.742163.
11. Kalafatakis, I., Kalafatakis, K., Tsimpolis, A., Giannakeas, N., Tsipouras, M., Tzallas, A., and Karagogeos, D. (2020). Using the Allen gene expression atlas of the adult mouse brain to gain further insight into the physiological significance of TAG-1/Contactin-2. Brain Struct. Funct. *225*, 2045–2056. https://doi.org/10.1007/s00429-020-02108-4.
12. Ruegg, M.A., Stoeckli, E.T., Kuhn, T.B., Heller, M., Zuellig, R., and Sonderegger, P. (1989). Purification of axonin-1, a protein that is secreted from axons during neurogenesis. EMBO J. *8*, 55–63.
13. Furley, A.J., Morton, S.B., Manalo, D., Karagogeos, D., Dodd, J., and Jessell, T.M. (1990). The axonal glycoprotein TAG-1 is an immunoglobulin superfamily member with neurite outgrowth-promoting activity. Cell *61*, 157–170.
14. Lierheimer, R., Kunz, B., Vogt, L., Savoca, R., Brodbeck, U., and Sonderegger, P. (1997). The neuronal cell-adhesion molecule axonin-1

is specifically released by an endogenous glycosylphosphatidylinositol-specific phospholipase. Eur. J. Biochem. *243*, 502–510.

15. Kuhn, P.H., Koroniak, K., Hogl, S., Colombo, A., Zeitschel, U., Willem, M., Volbracht, C., Schepers, U., Imhof, A., Hoffmeister, A., et al. (2012). Secretome protein enrichment identifies physiological BACE1 protease substrates in neurons. EMBO J. *31*, 3157–3168. https://doi.org/10.1038/emboj.2012.173.
16. Zhou, L., Barão, S., Laga, M., Bockstael, K., Borgers, M., Gijsen, H., Annaert, W., Moechars, D., Mercken, M., Gevaert, K., and De Strooper, B. (2012). The neural cell adhesion molecules L1 and CHL1 are cleaved by BACE1 protease *in vivo*. J. Biol. Chem. *287*, 25927–25940. https://doi.org/10.1074/jbc.M112.377465.
17. Gautam, V., D'Avanzo, C., Hebisch, M., Kovacs, D.M., and Kim, D.Y. (2014). BACE1 activity regulates cell surface contactin-2 levels. Mol. Neurodegener. *9*, 4. https://doi.org/10.1186/1750-1326-9-4.
18. Tachi, N., Hashimoto, Y., Nawa, M., and Matsuoka, M. (2010). TAG-1 is an inhibitor of TGFbeta2-induced neuronal death via amyloid beta precursor protein. Biochem. Biophys. Res. Commun. *394*, 119–125. https://doi.org/10.1016/j.bbrc.2010.02.127.
19. Okamoto, M., Namba, T., Shinoda, T., Kondo, T., Watanabe, T., Inoue, Y., Takeuchi, K., Enomoto, Y., Ota, K., Oda, K., et al. (2013). TAG-1-assisted progenitor elongation streamlines nuclear migration to optimize subapical crowding. Nat. Neurosci. *16*, 1556–1566. https://doi.org/10.1038/nn.3525.
20. Namba, T., Kibe, Y., Funahashi, Y., Nakamuta, S., Takano, T., Ueno, T., Shimada, A., Kozawa, S., Okamoto, M., Shimoda, Y., et al. (2014). Pioneering axons regulate neuronal polarization in the developing cerebral cortex. Neuron *81*, 814–829. https://doi.org/10.1016/j.neuron.2013.12.015.
21. Zou, D., Zhou, X., Liu, J., Zhao, Y., and Jiang, X. (2020). MiR-34a regulates Schwann cell proliferation and migration by targeting CNTN2. Neuroreport *31*, 1180–1188. https://doi.org/10.1097/wnr.0000000000001539.
22. Wolman, M.A., Sittaramane, V.K., Essner, J.J., Yost, H.J., Chandrasekhar, A., and Halloran, M.C. (2008). Transient axonal glycoprotein-1 (TAG-1) and laminin-alpha1 regulate dynamic growth cone behaviors and initial axon direction *in vivo*. Neural Dev. *3*, 6. https://doi.org/10.1186/1749-8104-3-6.
23. Wang, W., Karagogeos, D., and Kilpatrick, D.L. (2011). The effects of Tag-1 on the maturation of mouse cerebellar granule neurons. Cell. Mol. Neurobiol. *31*, 351–356. https://doi.org/10.1007/s10571-010-9641-6.
24. Dang, P., Smythe, E., and Furley, A.J.W. (2012). TAG1 regulates the endocytic trafficking and signaling of the semaphorin3A receptor complex. J. Neurosci. *32*, 10370–10382. https://doi.org/10.1523/JNEUROSCI.5874-11.2012.
25. Perrin, F.E., Rathjen, F.G., and Stoeckli, E.T. (2001). Distinct subpopulations of sensory afferents require F11 or axonin-1 for growth to their target layers within the spinal cord of the chick. Neuron *30*, 707–723.
26. Law, C.O., Kirby, R.J., Aghamohammadzadeh, S., and Furley, A.J.W. (2008). The neural adhesion molecule TAG-1 modulates responses of sensory axons to diffusible guidance signals. Development *135*, 2361–2371. https://doi.org/10.1242/dev.009019.
27. Suter, T.A.C.S., Blagburn, S.V., Fisher, S.E., Anderson-Keightly, H.M., D'Elia, K.P., and Jaworski, A. (2020). TAG-1 Multifunctionality Coordinates Neuronal Migration, Axon Guidance, and Fasciculation. Cell Rep. *30*, 1164–1177.e7. https://doi.org/10.1016/j.celrep.2019.12.085.
28. Savvaki, M., Kafetzis, G., Kaplanis, S.I., Ktena, N., Theodorakis, K., and Karagogeos, D. (2021). Neuronal, but not glial, Contactin 2 negatively regulates axon regeneration in the injured adult optic nerve. Eur. J. Neurosci. *53*, 1705–1721. https://doi.org/10.1111/ejn.15121.
29. Pinatel, D., Hivert, B., Boucraut, J., Saint-Martin, M., Rogemond, V., Zoupi, L., Karagogeos, D., Honnorat, J., and Faivre-Sarrailh, C. (2015). Inhibitory axons are targeted in hippocampal cell culture by anti-Caspr2 autoantibodies associated with limbic encephalitis. Front. Cell. Neurosci. *9*, 265. https://doi.org/10.3389/fncel.2015.00265.
30. Gonzalez-Lozano, M.A., Koopmans, F., Sullivan, P.F., Protze, J., Krause, G., Verhage, M., Li, K.W., Liu, F., and Smit, A.B. (2020). Stitching the synapse: Cross-linking mass spectrometry into resolving synaptic protein interactions. Sci. Adv. *6*, eaax5783. https://doi.org/10.1126/sciadv.aax5783.
31. Pinatel, D., Hivert, B., Saint-Martin, M., Noraz, N., Savvaki, M., Karagogeos, D., and Faivre-Sarrailh, C. (2017). The Kv1-associated molecules TAG-1 and Caspr2 are selectively targeted to the axon initial segment in hippocampal neurons. J. Cell Sci. *130*, 2209–2220. https://doi.org/10.1242/jcs.202267.
32. Poliak, S., Salomon, D., Elhanany, H., Sabanay, H., Kiernan, B., Pevny, L., Stewart, C.L., Xu, X., Chiu, S.Y., Shrager, P., et al. (2003). Juxtaparanodal clustering of Shaker-like K+ channels in myelinated axons depends on Caspr2 and TAG-1. J. Cell Biol. *162*, 1149–1160. https://doi.org/10.1083/jcb.200305018.
33. Traka, M., Goutebroze, L., Denisenko, N., Bessa, M., Nifli, A., Havaki, S., Iwakura, Y., Fukamauchi, F., Watanabe, K., Soliven, B., et al. (2003). Association of TAG-1 with Caspr2 is essential for the molecular organization of juxtaparanodal regions of myelinated fibers. J. Cell Biol. *162*, 1161–1172. https://doi.org/10.1083/jcb.200305078.
34. Savvaki, M., Theodorakis, K., Zoupi, L., Stamatakis, A., Tivodar, S., Kyriacou, K., Stylianopoulou, F., and Karagogeos, D. (2010). The expression of TAG-1 in glial cells is sufficient for the formation of the juxtaparanodal complex and the phenotypic rescue of tag-1 homozygous mutants in the CNS. J. Neurosci. *30*, 13943–13954. https://doi.org/10.1523/JNEUROSCI.2574-10.2010.
35. Rader, C., Stoeckli, E.T., Ziegler, U., Osterwalder, T., Kunz, B., and Sonderegger, P. (1993). Cell-cell adhesion by homophilic interaction of the neuronal recognition molecule axonin-1. Eur. J. Biochem. *215*, 133–141.
36. Tsiotra, P.C., Theodorakis, K., Papamatheakis, J., and Karagogeos, D. (1996). The fibronectin domains of the neural adhesion molecule TAX-1 are necessary and sufficient for homophilic binding. J. Biol. Chem. *271*, 29216–29222.
37. Malhotra, J.D., Tsiotra, P., Karagogeos, D., and Hortsch, M. (1998). Cis-activation of L1-mediated ankyrin recruitment by TAG-1 homophilic cell adhesion. J. Biol. Chem. *273*, 33354–33359.
38. Peng, Y.R., Tran, N.M., Krishnaswamy, A., Kostadinov, D., Martersteck, E.M., and Sanes, J.R. (2017). Satb1 Regulates Contactin 5 to Pattern Dendrites of a Mammalian Retinal Ganglion Cell. Neuron *95*, 869–883.e6. https://doi.org/10.1016/j.neuron.2017.07.019.
39. Kunz, B., Lierheimer, R., Rader, C., Spirig, M., Ziegler, U., and Sonderegger, P. (2002). Axonin-1/TAG-1 mediates cell-cell adhesion by a cis-assisted trans-interaction. J. Biol. Chem. *277*, 4551–4557.
40. Felsenfeld, D.P., Hynes, M.A., Skoler, K.M., Furley, A.J., and Jessell, T.M. (1994). TAG-1 can mediate homophilic binding, but neurite outgrowth on TAG-1 requires an L1-like molecule and beta 1 integrins. Neuron *12*, 675–690.
41. Kunz, S., Ziegler, U., Kunz, B., and Sonderegger, P. (1996). Intracellular signaling is changed after clustering of the neural cell adhesion molecules axonin-1 and NgCAM during neurite fasciculation. J. Cell Biol. *135*, 253–267.
42. Giger, R.J., Ziegler, U., Hermens, W.T., Kunz, B., Kunz, S., and Sonderegger, P. (1997). Adenovirus-mediated gene transfer in neurons: construction and characterization of a vector for heterologous expression of the axonal cell adhesion molecule axonin-1. J. Neurosci. Methods *71*, 99–111.
43. Pavlou, O., Theodorakis, K., Falk, J., Kutsche, M., Schachner, M., Faivre-Sarrailh, C., and Karagogeos, D. (2002). Analysis of interactions of the adhesion molecule TAG-1 and its domains with other immunoglobulin superfamily members. Mol. Cell. Neurosci. *20*, 367–381.
44. Kyriakopoulou, K., de Diego, I., Wassef, M., and Karagogeos, D. (2002). A combination of chain and neurophilic migration involving the adhesion molecule TAG-1 in the caudal medulla. Development *129*, 287–296.

45. Yamagata, M., and Sanes, J.R. (2012). Expanding the Ig superfamily code for laminar specificity in retina: expression and role of contactins. J. Neurosci. *32*, 14402–14414. https://doi.org/10.1523/JNEUROSCI.3193-12.2012.

46. Rader, C., Kunz, B., Lierheimer, R., Giger, R.J., Berger, P., Tittmann, P., Gross, H., and Sonderegger, P. (1996). Implications for the domain arrangement of axonin-1 derived from the mapping of its NgCAM binding site. Embo J *15*, 2056–2068.

47. Tzimourakas, A., Giasemi, S., Mouratidou, M., and Karagogeos, D. (2007). Structure-function analysis of protein complexes involved in the molecular architecture of juxtaparanodal regions of myelinated fibers. Biotechnol. J. *2*, 577–583.

48. Lu, Z., Reddy, M.V.V.V.S., Liu, J., Kalichava, A., Liu, J., Zhang, L., Chen, F., Wang, Y., Holthauzen, L.M.F., White, M.A., et al. (2016). Molecular Architecture of Contactin-associated Protein-like 2 (CNTNAP2) and its Interaction with Contactin 2 (CNTN2). J. Biol. Chem. *291*, 24133–24147. https://doi.org/10.1074/jbc.M116.748236.

49. Rubio-Marrero, E.N., Vincelli, G., Jeffries, C.M., Shaikh, T.R., Pakos, I.S., Ranaivoson, F.M., von Daake, S., Demeler, B., De Jaco, A., Perkins, G., et al. (2016). Structural Characterization of the Extracellular Domain of CASPR2 and Insights into Its Association with the Novel Ligand Contactin1. J. Biol. Chem. *291*, 5788–5802. https://doi.org/10.1074/jbc.M115.705681.

50. Liu, H., Focia, P.J., and He, X. (2011). Homophilic adhesion mechanism of neurofascin, a member of the L1 family of neural cell adhesion molecules. J. Biol. Chem. *286*, 797–805. https://doi.org/10.1074/jbc.M110.180281.

51. Gupta, R., and Brunak, S. (2002). Prediction of glycosylation across the human proteome and the correlation to protein function. Pac. Symp. Biocomput. 310–322.

52. Ashkenazy, H., Abadi, S., Martz, E., Chay, O., Mayrose, I., Pupko, T., and Ben-Tal, N. (2016). ConSurf 2016: an improved methodology to estimate and visualize evolutionary conservation in macromolecules. Nucleic Acids Res. *44*, W344–W350. https://doi.org/10.1093/nar/gkw408.

53. Chataigner, L.M.P., Gogou, C., den Boer, M.A., Frias, C.P., Thies-Weesie, D.M.E., Granneman, J.C.M., Heck, A.J.R., Meijer, D.H., and Janssen, B.J.C. (2022). Structural insights into the contactin 1 - neurofascin 155 adhesion complex. Nat. Commun. *13*, 6607. https://doi.org/10.1038/s41467-022-34302-9.

54. Jumper, J., Evans, R., Pritzel, A., Green, T., Figurnov, M., Ronneberger, O., Tunyasuvunakool, K., Bates, R., Žídek, A., Potapenko, A., et al. (2021). Highly accurate protein structure prediction with AlphaFold. Nature *596*, 583–589. https://doi.org/10.1038/s41586-021-03819-2.

55. Varadi, M., Anyango, S., Deshpande, M., Nair, S., Natassia, C., Yordanova, G., Yuan, D., Stroe, O., Wood, G., Laydon, A., et al. (2022). AlphaFold Protein Structure Database: massively expanding the structural coverage of protein-sequence space with high-accuracy models. Nucleic Acids Res. *50*, D439–D444. https://doi.org/10.1093/nar/gkab1061.

56. Meijers, R., Puettmann-Holgado, R., Skiniotis, G., Liu, J.H., Walz, T., Wang, J.H., and Schmucker, D. (2007). Structural basis of Dscam isoform specificity. Nature *449*, 487–491. https://doi.org/10.1038/nature06147.

57. Tang, H., Chang, H., Dong, Y., Guo, L., Shi, X., Wu, Y., Huang, Y., and He, Y. (2018). Architecture of cell-cell adhesion mediated by sidekicks. Proc. Natl. Acad. Sci. USA *115*, 9246–9251. https://doi.org/10.1073/pnas.1801810115.

58. Chataigner, L.M.P., Leloup, N., and Janssen, B.J.C. (2020). Structural Perspectives on Extracellular Recognition and Conformational Changes of Several Type-I Transmembrane Receptors. Front. Mol. Biosci. *7*, 129. https://doi.org/10.3389/fmolb.2020.00129.

59. Ma, Q.H., Futagawa, T., Yang, W.L., Jiang, X.D., Zeng, L., Takeda, Y., Xu, R.X., Bagnard, D., Schachner, M., Furley, A.J., et al. (2008). A TAG1-APP signalling pathway through Fe65 negatively modulates neurogenesis. Nat. Cell Biol. *10*, 283–294. https://doi.org/10.1038/ncb1690.

60. Gollan, L., Salomon, D., Salzer, J.L., and Peles, E. (2003). Caspr regulates the processing of contactin and inhibits its binding to neurofascin. J. Cell Biol. *163*, 1213–1218.

61. Bonnon, C., Bel, C., Goutebroze, L., Maigret, B., Girault, J.A., and Faivre-Sarrailh, C. (2007). PGY repeats and N-glycans govern the trafficking of paranodin and its selective association with contactin and neurofascin-155. Mol. Biol. Cell *18*, 229–241. https://doi.org/10.1091/mbc.E06-06-0570.

62. Labasque, M., Hivert, B., Nogales-Gadea, G., Querol, L., Illa, I., and Faivre-Sarrailh, C. (2014). Specific contactin N-glycans are implicated in neurofascin binding and autoimmune targeting in peripheral neuropathies. J. Biol. Chem. *289*, 7907–7918. https://doi.org/10.1074/jbc.M113.528489.

63. Rickman, D.S., Tyagi, R., Zhu, X.X., Bobek, M.P., Song, S., Blaivas, M., Misek, D.E., Israel, M.A., Kurnit, D.M., Ross, D.A., et al. (2001). The gene for the axonal cell adhesion molecule TAX-1 is amplified and aberrantly expressed in malignant gliomas. Cancer Res. *61*, 2162–2168.

64. Guo, Y., Zhang, P., Zhang, H., Zhang, P., and Xu, R. (2017). RNAi for contactin 2 inhibits proliferation of U87-glioma stem cells by downregulating AICD, EGFR, and HES1. OncoTargets Ther. *10*, 791–801. https://doi.org/10.2147/OTT.S113390.

65. Delgado, C., Bu, L., Zhang, J., Liu, F.Y., Sall, J., Liang, F.X., Furley, A.J., and Fishman, G.I. (2021). Neural Cell Adhesion Molecule Is Required for Ventricular Conduction System Development. Development *148*, dev199431. https://doi.org/10.1242/dev.199431.

66. Pallante, B.A., Giovannone, S., Fang-Yu, L., Zhang, J., Liu, N., Kang, G., Dun, W., Boyden, P.A., and Fishman, G.I. (2010). Contactin-2 expression in the cardiac Purkinje fiber network. Circulation *3*, 186–194. https://doi.org/10.1161/CIRCEP.109.928820.

67. Bhattacharyya, S., Bhakta, M., and Munshi, N.V. (2017). Phenotypically silent Cre recombination within the postnatal ventricular conduction system. PLoS One *12*, e0174517. https://doi.org/10.1371/journal.pone.0174517.

68. Savvaki, M., Panagiotaropoulos, T., Stamatakis, A., Sargiannidou, I., Karatzioula, P., Watanabe, K., Stylianopoulou, F., Karagogeos, D., and Kleopa, K.A. (2008). Impairment of learning and memory in TAG-1 deficient mice associated with shorter CNS internodes and disrupted juxtaparanodes. Mol. Cell. Neurosci. *39*, 478–490. https://doi.org/10.1016/j.mcn.2008.07.025.

69. Spead, O., Weaver, C.J., Moreland, T., and Poulain, F.E. (2021). Live Imaging of Retinotectal Mapping Reveals Topographic Map Dynamics and a Previously Undescribed Role for Contactin 2 in Map Sharpening. Development *148*, dev199584. https://doi.org/10.1242/dev.199584.

70. Saint-Martin, M., Pieters, A., Déchelotte, B., Malleval, C., Pinatel, D., Pascual, O., Karagogeos, D., Honnorat, J., Pellier-Monnin, V., and Noraz, N. (2019). Impact of anti-CASPR2 autoantibodies from patients with autoimmune encephalitis on CASPR2/TAG-1 interaction and Kv1 expression. J. Autoimmun. *103*, 102284. https://doi.org/10.1016/j.jaut.2019.05.012.

71. Soares, S., Traka, M., von Boxberg, Y., Bouquet, C., Karagogeos, D., and Nothias, F. (2005). Neuronal and glial expression of the adhesion molecule TAG-1 is regulated after peripheral nerve lesion or central neurodegeneration of adult nervous system. Eur. J. Neurosci. *21*, 1169–1180.

72. Lin, J.F., Pan, H.C., Ma, L.P., Shen, Y.Q., and Schachner, M. (2012). The cell neural adhesion molecule contactin-2 (TAG-1) is beneficial for functional recovery after spinal cord injury in adult zebrafish. PLoS One *7*, e52376. https://doi.org/10.1371/journal.pone.0052376.

73. Lang, D.M., Warren, J.T., Jr., Klisa, C., and Stuermer, C.A. (2001). Topographic restriction of TAG-1 expression in the developing retinotectal pathway and target dependent reexpression during axon regeneration. Mol. Cell. Neurosci. *17*, 398–414.

74. Kastriti, M.E., Stratigi, A., Mariatos, D., Theodosiou, M., Savvaki, M., Kavkova, M., Theodorakis, K., Vidaki, M., Zikmund, T., Kaiser, J., et al. (2019). Ablation of CNTN2+ Pyramidal Neurons During Development Results in Defects in Neocortical Size and Axonal Tract Formation. Front. Cell. Neurosci. *13*, 454. https://doi.org/10.3389/fncel.2019.00454.

75. Marell, P.S., Blohowiak, S.E., Evans, M.D., Georgieff, M.K., Kling, P.J., and Tran, P.V. (2019). Cord Blood-Derived Exosomal CNTN2 and BDNF: Potential Molecular Markers for Brain Health of Neonates at Risk

for Iron Deficiency. Nutrients *11*, 2478. https://doi.org/10.3390/nu11102478.

76. Derfuss, T., Parikh, K., Velhin, S., Braun, M., Mathey, E., Krumbholz, M., Kümpfel, T., Moldenhauer, A., Rader, C., Sonderegger, P., et al. (2009). Contactin-2/TAG-1-directed autoimmunity is identified in multiple sclerosis patients and mediates gray matter pathology in animals. Proc. Natl. Acad. Sci. USA *106*, 8302–8307. https://doi.org/10.1073/pnas.0901496106.
77. Boronat, A., Sepúlveda, M., Llufriu, S., Sabater, L., Blanco, Y., Gabilondo, I., Solà, N., Villoslada, P., Dalmau, J., Graus, F., and Saiz, A. (2012). Analysis of antibodies to surface epitopes of contactin-2 in multiple sclerosis. J. Neuroimmunol. *244*, 103–106. https://doi.org/10.1016/j.jneuroim.2011.12.023.
78. Chatterjee, M., Nöding, B., Willemse, E.A.J., Koel-Simmelink, M.J.A., van der Flier, W.M., Schild, D., and Teunissen, C.E. (2017). Detection of contactin-2 in cerebrospinal fluid (CSF) of patients with Alzheimer's disease using Fluorescence Correlation Spectroscopy (FCS). Clin. Biochem. *50*, 1061–1066. https://doi.org/10.1016/j.clinbiochem.2017.08.017.
79. Chatterjee, M., Del Campo, M., Morrema, T.H.J., de Waal, M., van der Flier, W.M., Hoozemans, J.J.M., and Teunissen, C.E. (2018). Contactin-2, a synaptic and axonal protein, is reduced in cerebrospinal fluid and brain tissue in Alzheimer's disease. Alzheimer's Res. Ther. *10*, 52. https://doi.org/10.1186/s13195-018-0383-x.
80. Chatterjee, M., Koel-Simmelink, M.J., Verberk, I.M., Killestein, J., Vrenken, H., Enzinger, C., Ropele, S., Fazekas, F., Khalil, M., and Teunissen, C.E. (2018). Contactin-1 and contactin-2 in cerebrospinal fluid as potential biomarkers for axonal domain dysfunction in multiple sclerosis. Mult. Scler. J. Exp. Transl. Clin. *4*, 2055217318819535. https://doi.org/10.1177/2055217318819535.
81. Zoupi, L., Savvaki, M., Kalemaki, K., Kalafatakis, I., Sidiropoulou, K., and Karagogeos, D. (2018). The function of contactin-2/TAG-1 in oligodendrocytes in health and demyelinating pathology. Glia *66*, 576–591. https://doi.org/10.1002/glia.23266.
82. Winter, G., Waterman, D.G., Parkhurst, J.M., Brewster, A.S., Gildea, R.J., Gerstel, M., Fuentes-Montero, L., Vollmar, M., Michels-Clark, T., Young, I.D., et al. (2018). DIALS: implementation and evaluation of a new integration package. Acta Crystallogr. D Struct. Biol. *74*, 85–97. https://doi.org/10.1107/S2059798317017235.
83. Evans, P.R., and Murshudov, G.N. (2013). How good are my data and what is the resolution? Acta Crystallogr. D *69*, 1204–1214. https://doi.org/10.1107/S0907444913000061.
84. Mccoy, A.J., Grosse-Kunstleve, R.W., Adams, P.D., Winn, M.D., Storoni, L.C., and Read, R.J. (2007). Phaser crystallographic software. J. Appl. Crystallogr. *40*, 658–674. https://doi.org/10.1107/S0021889807021206.
85. Du, Z., Su, H., Wang, W., Ye, L., Wei, H., Peng, Z., Anishchenko, I., Baker, D., and Yang, J. (2021). The trRosetta server for fast and accurate protein structure prediction. Nat. Protoc. *16*, 5634–5651. https://doi.org/10.1038/s41596-021-00628-9.
86. Afonine, P.V., Grosse-Kunstleve, R.W., Echols, N., Headd, J.J., Moriarty, N.W., Mustyakimov, M., Terwilliger, T.C., Urzhumtsev, A., Zwart, P.H., and Adams, P.D. (2012). Towards automated crystallographic structure refinement with phenix.refine. Acta Crystallogr. D Biol. Crystallogr. *68*, 352–367. https://doi.org/10.1107/S0907444912001308.
87. Emsley, P., and Cowtan, K. (2004). Coot: model-building tools for molecular graphics. Acta Crystallogr. D *60*, 2126–2132. https://doi.org/10.1107/S0907444904019158.
88. Williams, C.J., Headd, J.J., Moriarty, N.W., Prisant, M.G., Videau, L.L., Deis, L.N., Verma, V., Keedy, D.A., Hintze, B.J., Chen, V.B., et al. (2018). MolProbity: More and better reference data for improved all-atom structure validation. Protein Sci. *27*, 293–315. https://doi.org/10.1002/pro.3330.
89. Krissinel, E. (2015). Stock-based detection of protein oligomeric states in jsPISA. Nucleic Acids Res. *43*, W314–W319. https://doi.org/10.1093/nar/gkv314.
90. Hagemans, D., van Belzen, I.A.E.M., Morán Luengo, T., and Rüdiger, S.G.D. (2015). A script to highlight hydrophobicity and charge on protein surfaces. Front. Mol. Biosci. *2*, 56. https://doi.org/10.3389/fmolb.2015.00056.
91. Dolinsky, T.J., Nielsen, J.E., McCammon, J.A., and Baker, N.A. (2004). PDB2PQR: an automated pipeline for the setup of Poisson-Boltzmann electrostatics calculations. Nucleic Acids Res. *32*, W665–W667. https://doi.org/10.1093/nar/gkh381.
92. Baker, N.A., Sept, D., Joseph, S., Holst, M.J., and McCammon, J.A. (2001). Electrostatics of nanosystems: application to microtubules and the ribosome. Proc. Natl. Acad. Sci. USA *98*, 10037–10041. https://doi.org/10.1073/pnas.181342398.
93. UniProt Consortium (2021). UniProt: the universal protein knowledgebase in 2021. Nucleic Acids Res. *49*, D480–D489. https://doi.org/10.1093/nar/gkaa1100.
94. Filik, J., Ashton, A.W., Chang, P.C.Y., Chater, P.A., Day, S.J., Drakopoulos, M., Gerring, M.W., Hart, M.L., Magdysyuk, O.V., Michalik, S., et al. (2017). Processing two-dimensional X-ray diffraction and small-angle scattering data in DAWN 2. J. Appl. Crystallogr. *50*, 959–966. https://doi.org/10.1107/S1600576717004708.
95. Konarev, P.V., Volkov, V.V., Sokolova, A.V., Koch, M.H.J., and Svergun, D.I. (2003). PRIMUS: a Windows PC-based system for small-angle scattering data analysis. J. Appl. Crystallogr. *36*, 1277–1282. https://doi.org/10.1107/S0021889803012779.
96. Schneidman-Duhovny, D., Hammel, M., Tainer, J.A., and Sali, A. (2016). FoXS, FoXSDock and MultiFoXS: Single-state and multi-state structural modeling of proteins and their complexes based on SAXS profiles. Nucleic Acids Res. *44*, W424–W429. https://doi.org/10.1093/nar/gkw389.
97. Scheres, S.H.W. (2012). RELION: implementation of a Bayesian approach to cryo-EM structure determination. J. Struct. Biol. *180*, 519–530. https://doi.org/10.1016/j.jsb.2012.09.006.
98. Zhang, K. (2016). Gctf: Real-time CTF determination and correction. J. Struct. Biol. *193*, 1–12. https://doi.org/10.1016/j.jsb.2015.11.003.
99. Tang, G., Peng, L., Baldwin, P.R., Mann, D.S., Jiang, W., Rees, I., and Ludtke, S.J. (2007). EMAN2: an extensible image processing suite for electron microscopy. J. Struct. Biol. *157*, 38–46. https://doi.org/10.1016/j.jsb.2006.05.009.

STAR★METHODS

KEY RESOURCES TABLE

REAGENT or RESOURCE	SOURCE	IDENTIFIER
Bacterial and virus strains		
TOP10	Invitrogen	Cat# C404003
Chemicals, peptides, and recombinant proteins		
BamHI	New England Biolabs	Cat# R0136S
NotI	New England Biolabs	Cat# R0189S
Endo-H_f	New England Biolabs	Cat# P0703S
BglII	New England Biolabs	Cat# R0144S
HEPES	Sigma-Aldrich	Cat# H4043
Imidazole	Sigma-Aldrich	Cat# 56749
Sodium malonate	Sigma-Aldrich	Cat# M1875
Polyethylene glycol 3350	Sigma-Aldrich	Cat# 88276
Glycerol	VWR	Cat# 24388
Uranyl acetate	Gentaur	Cat# 671605
Critical commercial assays		
Q5 site-directed mutagenesis kit	New England Biolabs	Cat# E0554S
Superdex 200 Increase 10/300	GE Healthcare	Cat# 28990944
Superdex200 Hiload 16/600	GE Healthcare	Cat# 28989335
Ni Sepharose excel	GE Healthcare	Cat# 17371202
borosilicate capillaries	World Precision Instruments	Cat# 1B120F-4
Amicon Ultra 10 kDa MWCO spin-filter columns	Merck	Cat# UFC501096
Deposited data		
Crystal structure of contactin 2^{Ig1-6}	This study	PDB: 8A0Y
Contactin 2^{Ig1-6} HM 1 μM SAXS data	This study	SASBDB: SASDNP8
Contactin 2^{Ig1-6} HM 3 μM SAXS data	This study	SASBDB: SASDNQ8
Contactin 2^{Ig1-6} HM 6 μM SAXS data	This study	SASBDB: SASDNR8
Contactin 2^{Ig1-6} HM 13 μM SAXS data	This study	SASBDB: SASDNS8
Contactin 2^{Ig1-6} HM 26 μM SAXS data	This study	SASBDB: SASDNT8
Contactin 2^{Ig1-6} HM 52 μM SAXS data	This study	SASBDB: SASDNU8
Contactin 2^{Ig1-6} CG 1 μM SAXS data	This study	SASBDB: SASDNV8
Contactin 2^{Ig1-6} CG 3 μM SAXS data	This study	SASBDB: SASDNW8
Contactin 2^{Ig1-6} CG 5 μM SAXS data	This study	SASBDB: SASDNX8
Contactin 2^{Ig1-6} CG 11 μM SAXS data	This study	SASBDB: SASDNY8
Contactin 2^{Ig1-6} CG 24 μM SAXS data	This study	SASBDB: SASDNZ8
Contactin 2^{Ig1-6} CG 51 μM SAXS data	This study	SASBDB: SASDN29
Contactin 2^{fe} CG 1 μM SAXS data	This study	SASBDB: SASDN39
Contactin 2^{fe} CG 2 μM SAXS data	This study	SASBDB: SASDN49
Contactin 2^{fe} CG 3 μM SAXS data	This study	SASBDB: SASDN59
Contactin 2^{fe} CG 6 μM SAXS data	This study	SASBDB: SASDN69
Contactin 2^{fe} CG 12 μM SAXS data	This study	SASBDB: SASDN79
Contactin 2^{fe} CG 23 μM SAXS data	This study	SASBDB: SASDN89
Contactin 2^{fe} CG 50 μM SAXS data	This study	SASBDB: SASDN99
Experimental models: Cell lines		
HEK293 (EBNA)	ImmunoPrecise Antibodies	N/A
HEK293 GnTI$^-$ (EBNA)	ImmunoPrecise Antibodies	N/A

(*Continued on next page*)

Continued

REAGENT or RESOURCE	SOURCE	IDENTIFIER
Oligonucleotides		
Oligonucleotides are listed in Table S2	This study	N/A
Recombinant DNA		
Contactin 2	Image Clone	Image:30362931
Contactin 1	Image Clone	Image:30099512
Software and algorithms		
DLS processing pipeline	Winter et al.[82]	https://www.diamond.ac.uk/Instruments/Mx/I03/I03-Manual/Data-Analysis/Automated-Software-Pipeline.html
Aimless	Evans and Murshudov[83]	https://www.mrc-lmb.cam.ac.uk/harry/pre/aimless.html
Coot	Emsley and Cowtan[87]	https://www2.mrc-lmb.cam.ac.uk/personal/pemsley/coot
PyMol	Schrödinger	https://pymol.org/2/
Phenix	Adams et al.[86]	http://www.phenix-online.org/
Phaser	McCoy et al.[84]	https://www.phaser.cimr.cam.ac.uk/index.php/Phaser_Crystallographic_Software
tr-Rosetta	Du et al.[85]	https://yanglab.nankai.edu.cn/trRosetta/
Molprobity	Williams et al.[88]	http://molprobity.biochem.duke.edu/
jsPISA	Krissinel[89]	https://www.ccp4.ac.uk/pisa/
PDB2PQR	Dolinsky et al.[91]	https://www.cgl.ucsf.edu/chimera/docs/ContributedSoftware/apbs/pdb2pqr.html
APBS	Baker et al.[92]	https://apbs.readthedocs.io/en/latest/
CONSURF	Ashkenazy et al.[52]	http://consurf.tau.ac.il/
UNIPROT	Uniprot Consortium[93]	https://www.uniprot.org/
DAWN	Filik et al.[94]	https://www.diamond.ac.uk/Science/Research/Highlights/2017/DAWN-2.html
PRIMUS	Konarev et al.[95]	https://www.embl-hamburg.de/biosaxs/primus.html
FoXS	Schneidman-Duhovny et al.[96]	https://modbase.compbio.ucsf.edu/foxs/
RELION	Scheres[97]	https://relion.readthedocs.io/en/release-4.0/
gCTF	Zhang[98]	https://www2.mrc-lmb.cam.ac.uk/download/gctf/
EMAN2	Tang et al.[99]	https://blake.bcm.edu/emanwiki/EMAN2
MassLynx V4.1	Waters	https://www.waters.com/waters/en_US/MassLynx-Mass-Spectrometry-Software-/nav.htm
ASTRA6	Wyatt Technology	https://www.wyatt.com/products/software/astra.html

RESOURCE AVAILABILITY

Lead contact

Further information and requests for resources and reagents should be directed to and will be fulfilled by the lead contact, Bert Janssen (b.j.c.janssen@uu.nl).

Materials availability

Plasmids are available through ImmunoPrecise Antibodies with a completed Material Transfer Agreement. All other unique/stable reagents generated in this study are available from the lead contact with a completed Materials Transfer Agreement.

Data and code availability

- Coordinates and structure factors for contactin $2^{Ig1\text{-}6}$ have been deposited at the Protein Data Bank with accession number 8A0Y and are publicly available as of the date of publication. All SAXS data have been deposited at the small-angle scattering

biological data bank (SASBDB) and are publicly available as of the date of publication. Accession numbers are listed in the key resources table.

- This paper does not report original code.
- Any additional information required to reanalyze the data reported in this paper is available from the lead contact upon request.

EXPERIMENTAL MODEL AND STUDY PARTICIPANT DETAILS

Cell lines

HEK293 cells were used for recombinant protein expression. Transfected HEK293 cells that stably express Epstein-Barr virus nuclear antigen (EBNA) (HEK293-E, ImmunoPrecise Antibodies), and N-acetylglucoaminyltransferase I (GnTI)-deficient HEK293-Epstein-Barr virus nuclear antigen (EBNA1) expressing cells (HEK293-ES, ImmunoPrecise Antibodies) were grown for five days in suspension in FreeStyle medium (Invitrogen, Cat#12338026) at 37°C, with humidified atmosphere of 5% CO2.

Microbe strains

E. coli TOP10 cells were used for plasmid production and grown overnight at 37°C in lysogeny broth (LB) medium.

METHOD DETAILS

Construct generation and mutagenesis

Contactin 2 (CNTN2) based on Image Clone 30362931, was used as template to generate contactin $2^{Ig1\text{-}6}$ (residues 29-608) and contactin 2^{fe} (residues 29-1004) constructs by polymerase chain reaction (PCR). The contactin 1^{fe} (residues 21-996) construct was generated from CNTN1 Image Clone 30099512. Mutants were created using overlapping primers. All constructs were subcloned using BamHI/NotI sites into pUPE107.03 (cystatin secretion signal peptide, C-terminal His6 tag, ImmunoPrecise Antibodies).

Protein expression and purification

Complex glycan (CG) containing proteins were produced in suspension preparations of Epstein–Barr virus nuclear antigen I (EBNA1)-expressing HEK293 cells (HEK293-E), while high-mannose (HM) proteins were produced in N-acetylglucoaminyltransferase I-deficient (GnTI−) EBNA1-expressing HEK293 cells (HEK293-ES) (ImmunoPrecise Antibodies). Medium was harvested six days after transfection and cells were spun down by 10 min of centrifugation at 1000 × g. Cellular debris was then spun down from medium for 15 minutes at 4000 × g. Protein was purified using Ni Sepharose excel (GE Healthcare) affinity chromatography followed by size exclusion chromatography (SEC) on either Superdex200 Hiload 16/600 (GE Healthcare) or Superdex200 10/300 (GE Healthcare) columns equilibrated in SEC buffer (25 mM HEPES pH 7.5, 150 mM NaCl) for contactin $2^{Ig1\text{-}6}$ and contactin 1^{fe}, and IMAC buffer (25 mM HEPES pH 7.5, 500 mM NaCl, 500 mM Imidazole) for contactin 2^{fe}. Protein was then concentrated to 5-10 mg ml^{-1} and stored at -80°C. Purity was evaluated by SDS-PAGE and Coomassie staining.

Crystallization and X-ray data collection

Initial crystallization attempts yielded poorly diffracting contactin $2^{Ig1\text{-}6}$ crystals. De-glycosylation was performed to enhance crystallization by adding Endo-H_f (1.0×10^6 U ml^{-1}, New England Biolabs) 1:100 (v per v) directly to the concentrated protein 2 hours prior to setting up crystallization screening. Sitting-drop vapour diffusion at 4°C was used for all crystallization trials, by mixing 150 nl of protein solution (8 mg ml^{-1}) in SEC buffer with 150 nl of reservoir solution. Crystals of contactin $2^{Ig1\text{-}6}$ grew from a condition with 0.1 M Sodium malonate pH 6.0 and 12% w/v Polyethylene glycol 3,350. Reservoir solution supplemented with 30% of glycerol was added as cryo-protectant to the crystals before plunge freezing them in liquid nitrogen. Contactin $2^{Ig1\text{-}6}$ data sets were collected at 100K at Diamond Light Source beamline I03 at a wavelength of 0.9762Å.

Structure determination and refinement

Unmerged and unscaled integrated diffraction data were obtained for contactin $2^{Ig1\text{-}6}$ from the diamond beamline data auto processing pipeline[82] for two isomorphic contactin $2^{Ig1\text{-}6}$ datasets collected in succession from the same crystal. These data were combined, scaled, merged and further processed in *AIMLESS*.[83] Resolution limit cut off was determined based on mean intensity correlation coefficient of half-data sets, CC1/2. The structure was solved by molecular replacement using *PHASER*.[84] Initial search models for contactin $2^{Ig1\text{-}6}$ were (PDB: 2OM5)[7] for contactin 2 Ig1-4 residues 31-437 and *tr-Rosetta*[85] generated models for Ig5 (TM-score: 0.937) and Ig6 (TM-score: 0.936) domains. Structure refinement was performed using *PHENIX*[86] with automatic weighting options, and manual model building, aided by the high solvent content of the crystals of 78%, was performed in *COOT*.[87] To minimize overfitting, secondary structure, local NCS, and reference model restraints using (PDB: 2OM5)[7] and (PDB: 5I99)[10] were applied. Given observed mobility of domains between chains within the dataset, per domain TLS parameters were set additionally to individual isotropic B-factors. *MOLPROBITY*[88] was used for structure validation. Dataset and refinement statistics are provided in Table 1.

Structural analyses

Structural analyses were performed using various programs. Interface properties and buried surface areas were determined with the *jsPISA*[89] server. Hydrophobic surface representation coloring was obtained using the YRB coloring scheme.[90] Electrostatic surface properties at pH 7.4 were obtained using the *PDB2PQR*[91] and *APBS*[92] webservers. Conservation analyses were performed using *CONSURF*[52] with curated sequence lists retrieved for vertebrate orthologues from the UNIPROT[93] database. Figures were generated with *PyMol* (Schrödinger).

Small-angle X-ray scattering

Batch SAXS experiments were carried out at the Diamond Light Source (DLS) beamline B21 operating at an energy of 12.4 keV and using a sample-to-detector (Eiger 4M, Dectris) distance of 4.01 m. Scattering of pure water was used to calibrate the intensity to absolute units. Data reduction was performed automatically using the *DAWN*[94] pipeline. Frames were averaged after manual inspection for radiation damage, scattering of SEC buffer for contactin $2^{Ig1\text{-}6}$ and IMAC buffer for contactin 2^{fe} were subtracted, and intensities were normalized by protein sample concentration (Table 3). Data was analyzed in *PRIMUS*[95] and results were plotted in *EXCEL* (Microsoft). Expected monomer molecular weights for oligomerization analyses were estimated from sequence derived molecular weight, adding 1.5 kDa or 2 kDa per predicted glycosylation sites for high mannose and complex glycan material, respectively. P(r) analyses values were not determined given the non-monodispersity of samples. Rg values were calculated from the monomer and oligomer structures present in the contactin $2^{Ig1\text{-}6}$ crystal using the *FoXS*[96] webserver. To reflect the glycosylation state of these structures, and to allow comparison with the SAXS data, high-mannose glycans were modelled at glycosylation sites using geometric restraints in *COOT*.[87] Two variations in the orientation of the glycan position with respect to the protein were generated; one version in which the entire glycan trees were positioned closer to the protein surface, denoted ‘‘closer’’ and one version in which the glycan trees were pointing away from the protein surface, denoted ‘‘looser’’ (Table S1).

SEC-MALS

SEC analysis was performed on contactin $2^{Ig1\text{-}6}$ HM and CG samples to characterize oligomer exchange through peak shift. Purified samples (4-120 μM) were injected onto a Superdex200 10/300 increase (GE Healthcare) column equilibrated in SEC buffer and separated with a flow rate of 0.40 ml min−1. For sample molecular weight characterization, light scattering measurements were performed using a miniDAWN TREOS multiangle light scattering detector (Wyatt), connected to a differential refractive index monitor (Shimadzu, RID-10A) used in protein concentration quantification. Collected chromatograms were analyzed and processed using ASTRA6 software (Wyatt) using a calculated dn/dc value of 0.180 ml g^{-1} and 0.178 ml g^{-1} for HM and CG material respectively, determined from dn/dc of 0.186 and 0.140 for the protein and glycan parts respectively, and 14% (w/w HM) and 18% (w/w CG) glycosylation calculated from 7 crystallographically confirmed glycosylation sites. Instrument calibration was assessed by injection of 5 mg mL^{-1} monomeric conalbumin (Sigma-Aldrich).

Negative stain electron microscopy

4 μl of contactin 2^{fe} sample in IMAC buffer diluted ~1200 fold with SEC buffer to 5.0 μg/ml (39 nM) protein concentration was applied to glow discharged carbon coated copper grids. After 60 s the excess sample was removed with blotting paper and the grids were stained 2x 10 s with 2 % uranyl acetate solution. Electron micrographs were acquired on a Tecnai 20 electron microscope with LaB6 filament, operating at 200 kV, equipped with a BM Eagle 4K CCD camera at a nominal magnification of 100 000 x and a defocus of 1.5 μm. For 2D classification new grids were prepared using 10 μg/ml protein in SEC buffer and micrographs were recorded on a Talos L120C at 120 kV using a Ceta CMOS camera at 92 000 x magnification resulting in a pixel size of 1.55 Å/pixel.

Image processing for 2D classification

2000 particles were manually picked from 38 micrographs in RELION[97] and the contrast transfer function (CTF) per micrograph was estimated using gCTF.[98] Reference-free 2D class averaging of four times down sampled images was performed in RELION with 50 classes and a mask of 300 Å in diameter. Calculated projections of rigid-body models were generated with EMAN2,[99] either filtered to 20 Å (Figure 5G) or unfiltered (Figure S7).

Native mass spectrometry

A total amount of 50 μg protein was buffer exchanged into 150 mM ammonium acetate buffer pH 7.5, using 10 kDa MWCO spin-filter columns (Amicon Ultra centrifugal filters 10 K MWCO). After buffer exchange, the concentrations of the solutions were quantified by measuring the absorbance at 280 nm using a NanoDrop One instrument (Thermo Fisher). All samples were subsequently diluted to a concentration of 0.3 mg/ml (4 μM). The analysis of these samples was conducted using a modified LCT time-of-flight instrument (Waters). Nanoelectrospray needles were prepared in-house from borosilicate capillaries (World Precision Instruments), using a Sutter P-97 puller (Sutter Instrument) to pull needle tips, and an Edwards Scancoat Six sputter coater (Edwards Laboratories) to apply the gold coating. Sample aliquots of 2 μL were loaded into nanoelectrospray needles for measurements using a static spray. Consistency in measurement conditions was ensured, with parameters set as follows: the capillary was maintained within the range of 1400-1500 V, the sample cone voltage was 75 V, the extraction cone 0 V and a backing pressure of 6 mbar was applied. Acquired data was processed in MassLynx V4.1 (Waters).

QUANTIFICATION AND STATISTICAL ANALYSIS

A summary of data collection and refinement statistics for diffraction data is reported in Table 1. Quantification of the small-angle X-ray scattering (SAXS) data was performed using *PRIMUS*[95] and standard deviations are provided with the estimated radius of gyration value. A summary of the SAXS data statistics is reported in Table 3. Statistical analysis of the MALS data was performed using ASTRA6 software (Wyatt) and weight-average molar mass (Mw) data are expressed as the average ± SD and reported in Table 2.

Structure, Volume *32*

Supplemental Information

Contactin 2 homophilic adhesion structure and conformational plasticity

Lucas M.P. Chataigner, Lena Thärichen, J. Wouter Beugelink, Joke C.M. Granneman, Nadia J. Mokiem, Joost Snijder, Friedrich Förster, and Bert J.C. Janssen

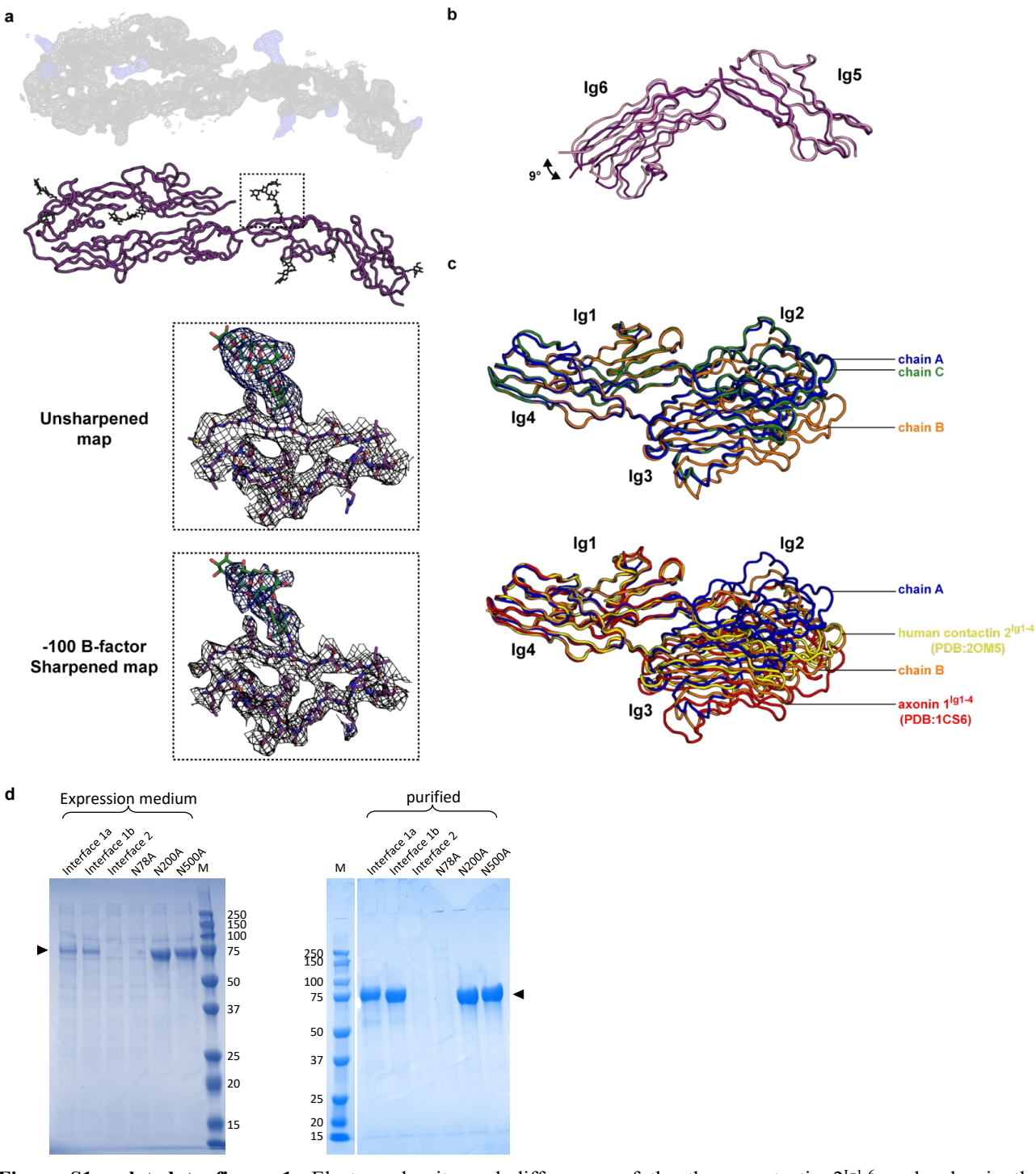

Figure S1, related to figure 1: Electron density and differences of the three contactin 2^{Ig1-6} molecules in the asymmetric unit. **a** (top) Electron density ($2mF_{obs}$-DF_{calc}) at 1σ of contactin 2^{Ig1-6} from a crystal that diffracted to a maximum resolution of 3.5 Å with chain density shown in black and glycan density shown in blue, and ribbon representation with glycans illustrating sufficient electron density for modelling. Unsharpened and -100 $Å^2$ B-factor sharpened local electron density around glycosylated asn 500 (bottom panels). **b** Superposed Ig5-Ig6 from conformationally distinct contactin 2^{Ig1-6} showing Ig6 hinges 9° off Ig5 at the Ig5-Ig6 connection. **c** Comparison of horseshoe bending motion between chains A-C in the contactin 2^{Ig1-6} dataset and chicken and human contactin 2^{Ig1-4} structures. **d** Expression level and purification of contactin 2^{Ig1-6} mutants used in this study. Interface 1a is R169D, F175D, F178D, L210D, interface 1b is F175D, F178D, and interface 2 is L332D, A353D, R508D, M540D. Interface 1a and b are mutations in the Ig1-2 interface and interface 2 are mutations in the Ig3-6 interface. Contactin 2^{Ig1-6} bands are indicated by black arrowheads next to the gels. The white line in the right gel indicates removal of irrelevant lanes. The interface 2 and N78A mutants are not secreted by the HEK293 cells.

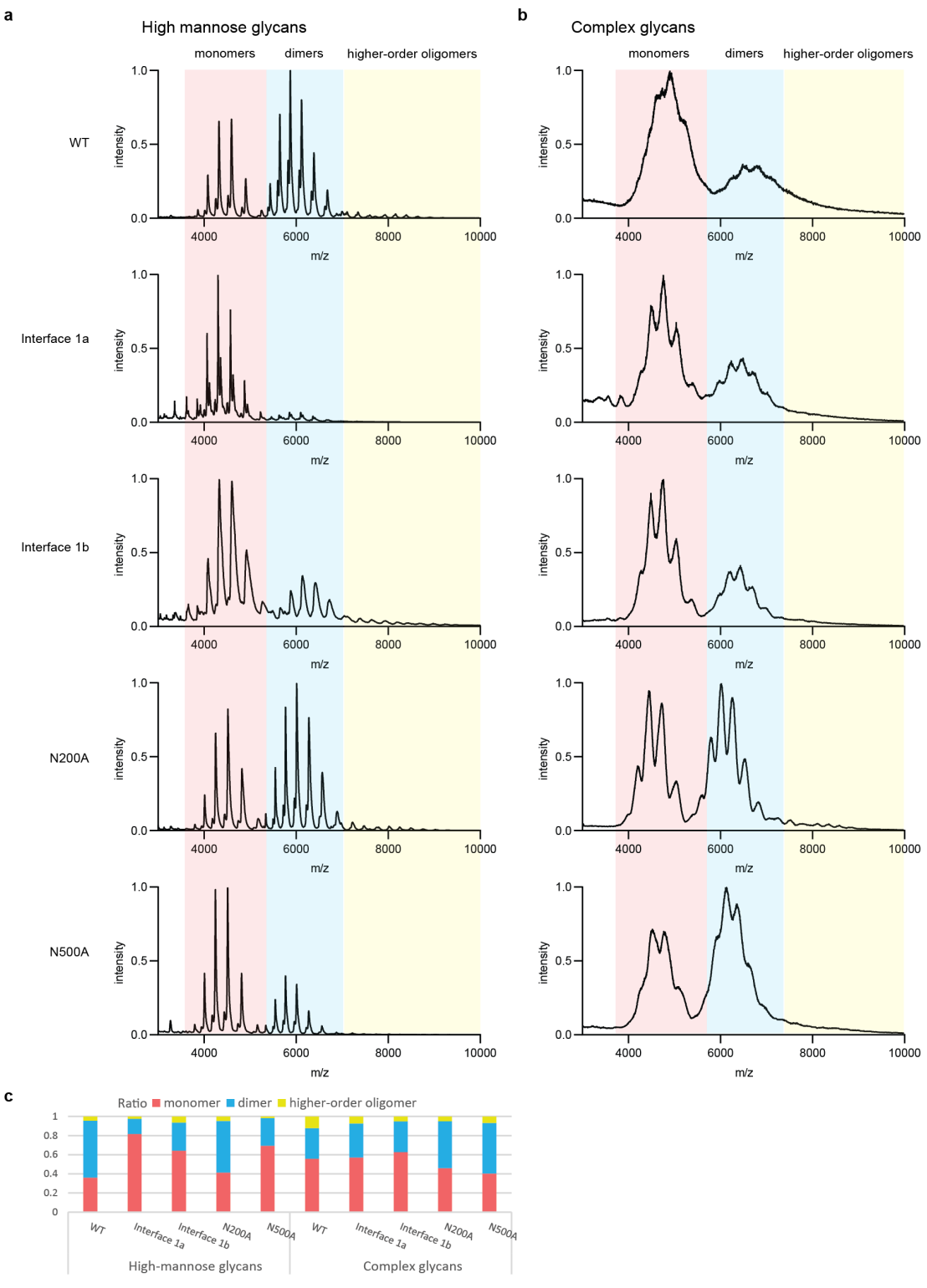

Figure S2, related to table 4: Dimerization of contactin $2^{Ig1\text{-}6}$ is glycan and glycan-type dependent. **a** Contactin $2^{Ig1\text{-}6}$ variants with high-mannose glycans and, **b** with complex-type glycans analysed by native mass spectrometry. **c** Ratios between monomer, dimer and higher-order oligomers determined from **a** and **b**. In all variants, monomers, dimers and higher-order oligomers are present. Wt contactin $2^{Ig1\text{-}6}$ with complex glycans contains the largest fraction of oligomers. The Ig1-2 interface mutants, interface 1a and 1b, lead to less dimer formation in the high-mannose but not in complex-glycan contactin $2^{Ig1\text{-}6}$. Deletion of the glycan on N500 reduces dimerization of high-mannose contactin $2^{Ig1\text{-}6}$. Deletion of the glycan on N200 or on N500 increases dimerization of complex-glycan contactin $2^{Ig1\text{-}6}$.

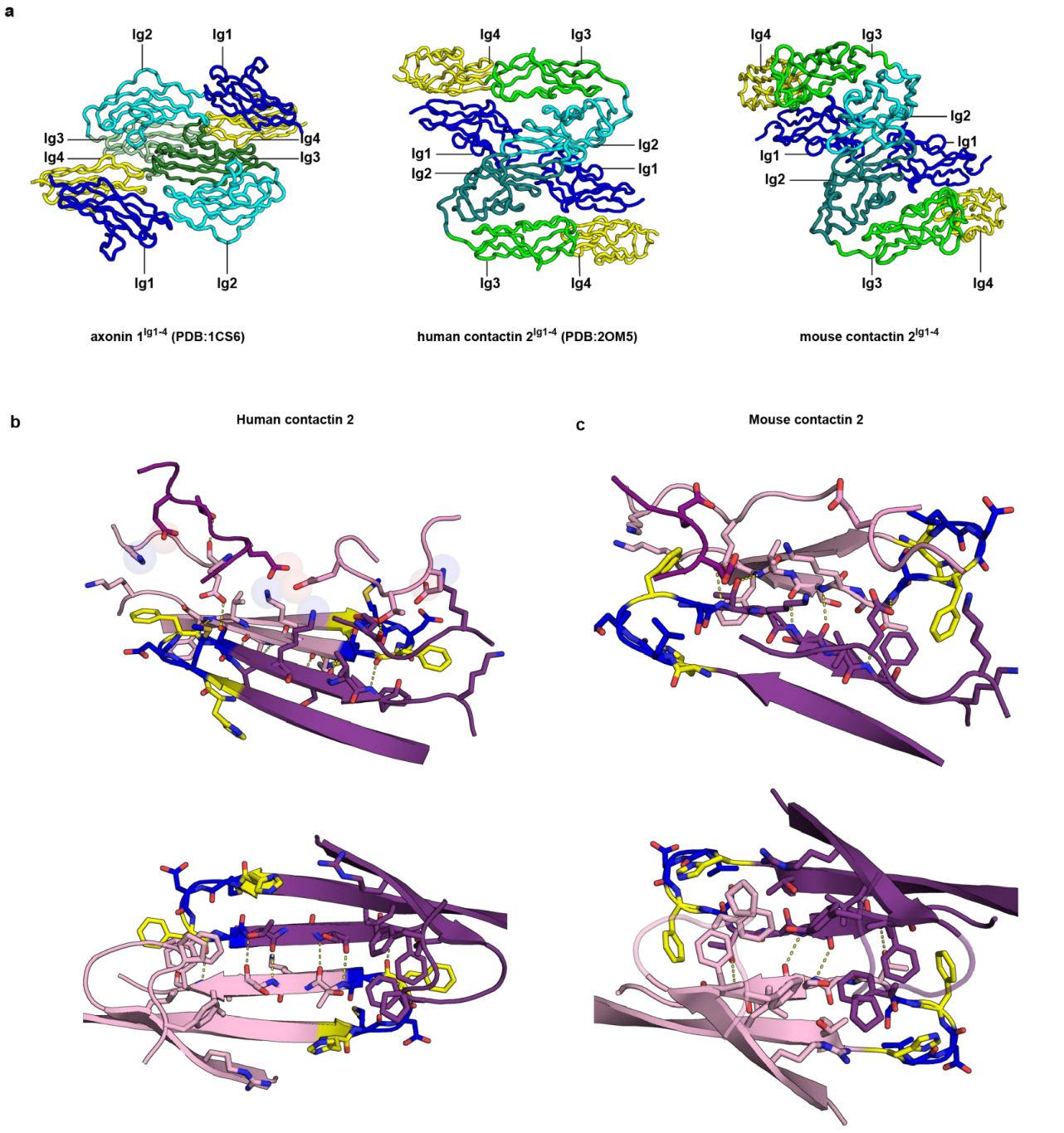

Figure S3, related to figure 3: The interaction mode of chicken contactin 2 differs from that of human and mouse contactin 2. **a** Side by side of chicken contactin $2^{Ig1\text{-}4}$ Ig1-4 zipper interaction mode, and human and mouse contactin $2^{Ig1\text{-}4}$ Ig1-2 dimer interaction modes. **b-c** FG loop deletion mutation (blue) and double mutant (yellow) abrogating cell clumping are located in the human (**b**) in and the mouse (**c**) Ig1-2 dimer interface. Top and bottom panels represent two different views. Dimer colored as in fig. 2a.

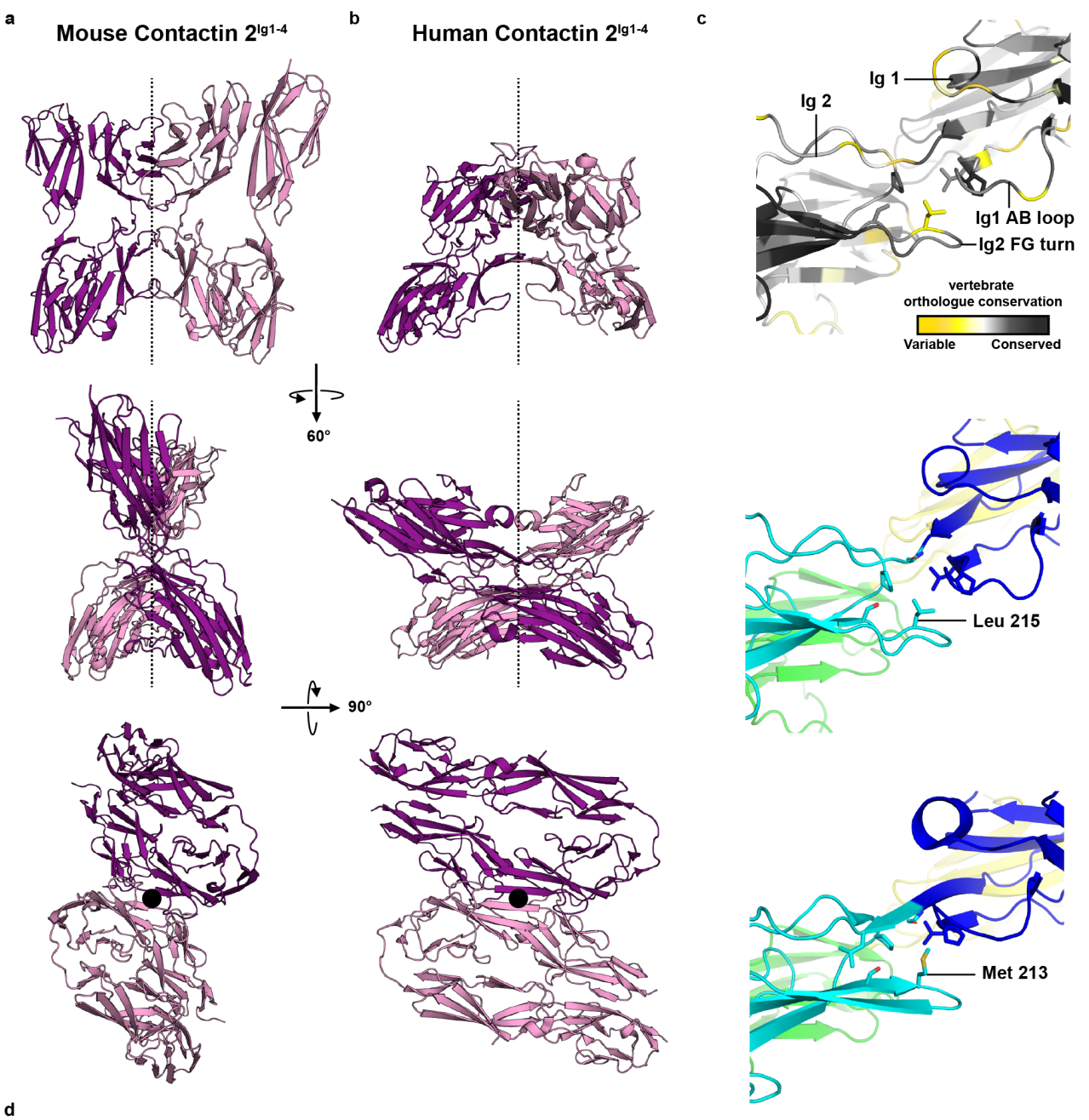

d

```
human    26 SALGSQTTFGPVFEDQPLSVLFPEESTEEQVLLACRARASPPATYRWKMNGTEMKLEPGSRHQLVGGNLVIMNPTKAQDAGVYQCLASNPVGTVVSREAILRFG 129
mouse    29 FSQGTPATFGPVFEEQPVGLLFPEESAEDQVTLACRARASPPATYRWKMNGTEMNLEPGSRHQLMGGNLVIMSPTKAQDAGVYQCLASNPVGTVVSKEAVLRFG 132
               : *: :*******:**: :******:*:** **********************:*********:******* ************************:**:****

human   130 FLQEFSKEERDPVKTHEGWGVMLPCNPPAHYPGLSYRWLLNEFPNFIPTDGRHFVSQTTGNLYIARTNASDLGNYSCLATSHMDFSTKSVFSKFAQLNLAAEDT 233
mouse   133 FLQEFSKEERDPVKTHEGWGVMLPCNPPAHYPGLSYRWLLNEFPNFIPTDGRHFVSQTTGNLYIARTNASDLGNYSCLATSHLDFSTKSVFSKFAQLNLAAEDP 236
            ********************************************************************************:********************
```

Figure S4, related to figure 3: Mouse and human contactin 2 interaction modes are of similar architecture but have differences as well. **a** Three views of mouse contactin 2^{Ig1-4} Ig1-2 dimer interaction mode. **b** Three views of human contactin 2^{Ig1-4} (PDB:2OM5) Ig1-2 dimer interaction mode. **c** Mouse contactin 2 Ig1 – Ig2 intramolecular interface colored by conservation, with black residues more conserved and yellow residues less conserved (top). Difference in Ig1-2 intramolecular interface between mouse (middle) and human (bottom) could help explain differences in interaction modes observed. **d** Sequence alignment of Ig1-2 of human and mouse contactin 2. The Ig1 AB loop (green) and the Ig2 FG turn (cyan) are highlighted. Conserved residues are indicated by * and similar residues by :.

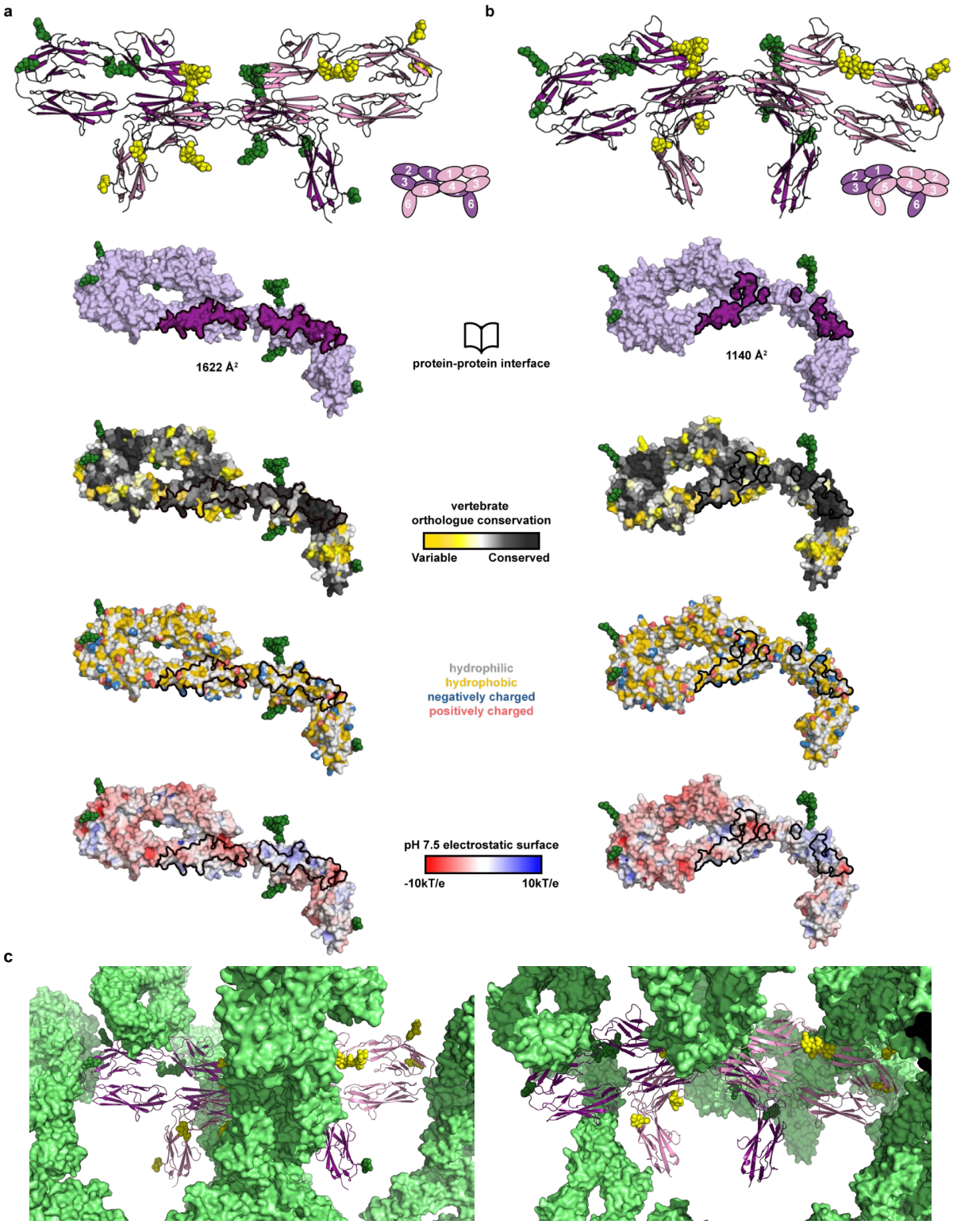

Figure S5, related to figure 4: Comparison of surface properties for conformationally distinct Ig3-6 contactin $2^{Ig1\text{-}6}$ dimers. **a** Cartoon representation of contactin $2^{Ig1\text{-}6}$ Ig3-6 mediated dimer in spread conformation and associated open book surface representations. **b** Cartoon representation of contactin $2^{Ig1\text{-}6}$ Ig3-6 mediated dimer in strained conformation and associated open book surface representations. **c** Lattice contacts are different for the two independent Ig3-6 dimers in the crystal. Symmetry related molecules are shown in surface representation.

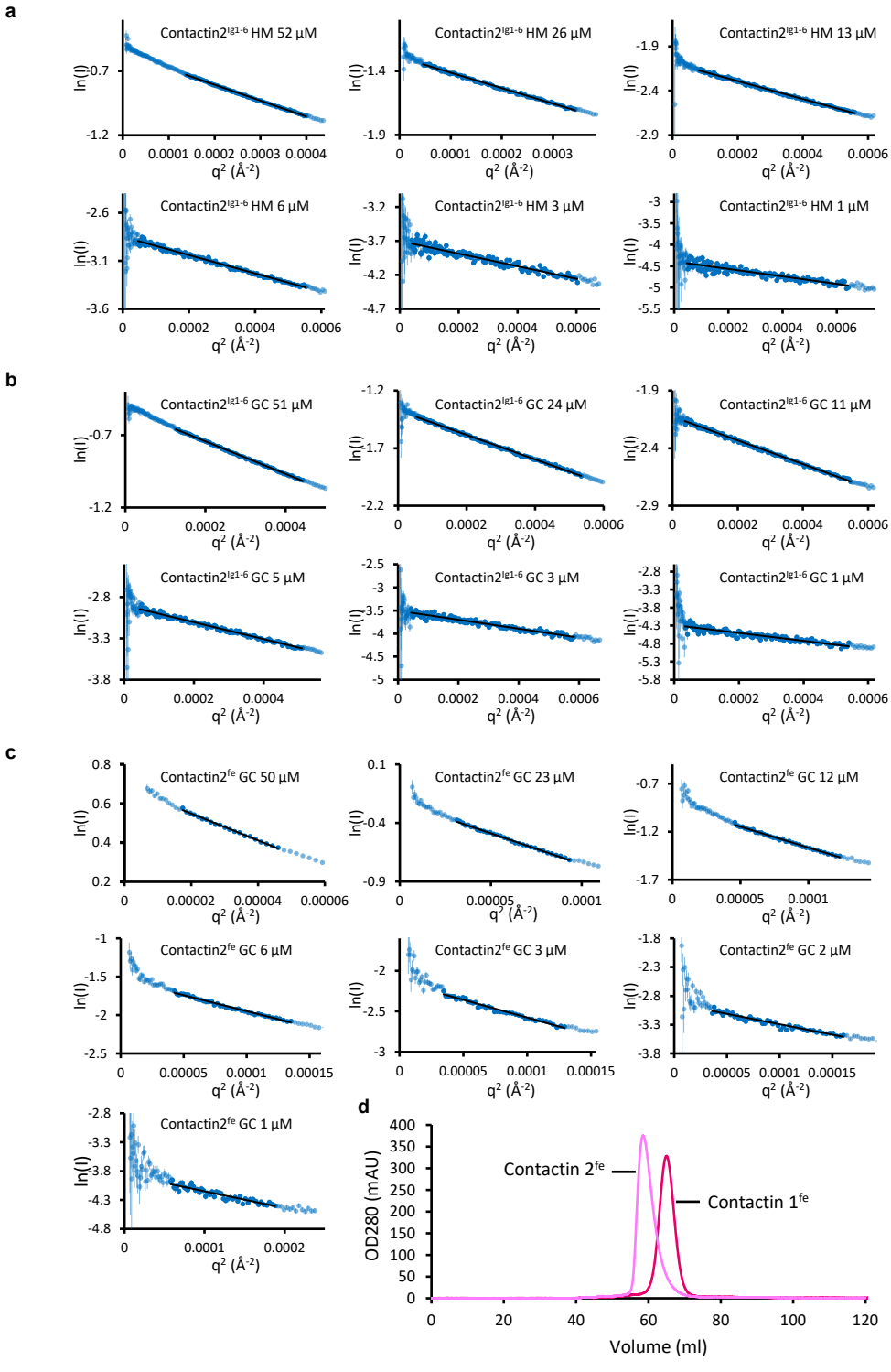

Figure S6, related to table 3: SAXS-based Guinier plots including linear fits from which I_0, molecular weight from I_0 and R_g have been derived. **a-c** SAXS-based Guinier plots with fits shown as black line. Light symbols represent data not used for fitting. The Ig1-6 contactin 2 variants with high mannose glycans (**a**) and complex glycans (**b**), and the full-ectodomain contactin 2 variant with complex glycans (**c**) are shown at different concentrations. The I_0, molecular weight from I_0 and R_g, determined from the fits are reported in Table 3. **d** Size-exclusion chromatography comparison of full-ectodomain contactin 1 and contactin 2. Contactin 2 elutes with a smaller retention volume and is thus likely an oligomer, whereas contactin 1 elutes as a monomer [S1].

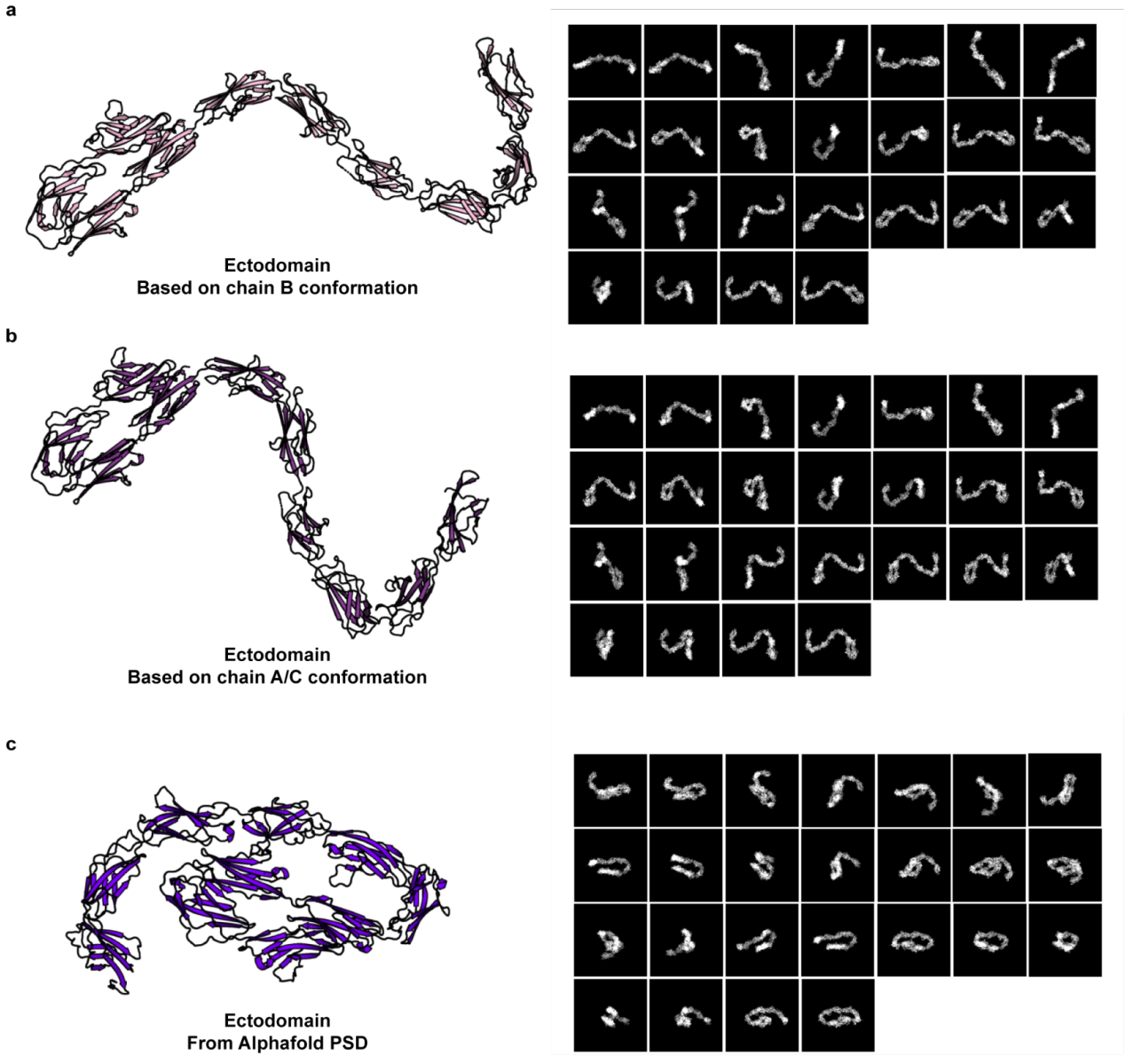

Figure S7, related to figure 5: Calculated 2D projections for contactin ectodomain models. **a,b** Models produced using partial structures and various chains of contactin $2^{Ig1\text{-}6}$. **c** Model available from the alphafold PSD. Interestingly, the projections from **a** and **b** match better than those of **c** to the class averages as reported in Fig. 5d.

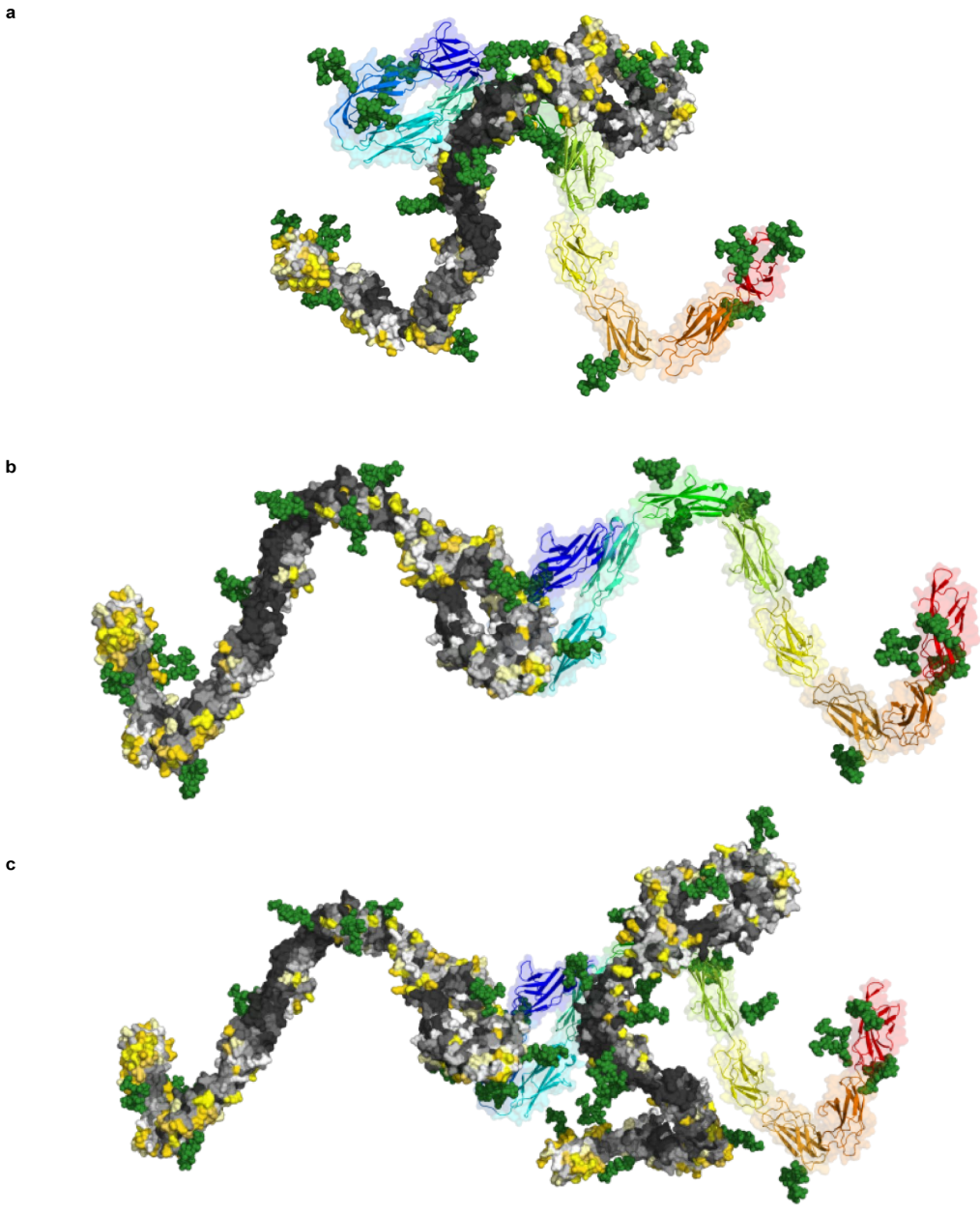

Figure S8, related to figure 5: Ectodomain models of contactin 2^{fe} colored with either conservation coloring or rainbow coloring per domain, modeled into Ig3-6 mediated dimer, Ig1-2 mediated dimer, or trimer arrangement combining both dimers. The dimers and trimer are compatible with *cis* or *trans* cellular interactions considering the presence of some flexion in domain connections.

Table S1, related to table 3: Calculated Rg for contactin 2^{Ig1-6} oligomer models with glycans closer to or pointing away from the protein surface.

Contactin 2^{Ig1-6} model	Chains	Mannose modelled glycans	Calculated Rg (nm)
Monomer	A	Looser	4.73
		Closer	4.66
	B	Looser	4.70
		Closer	5.13
	C	Looser	5.17
		Closer	4.67
Dimer 1	AB	Looser	6.59
		Closer	6.55
	CC	Looser	6.49
		Closer	6.47
Dimer 2	AC	Looser	5.36
		Closer	5.31
	BB	Looser	5.64
		Closer	5.61
Trimer	ABC	Looser	7.27
		Closer	7.25
	ACC	Looser	7.26
		Closer	7.23
	BBA	Looser	7.15
		Closer	7.12

Table S2, related to STAR Methods: Oligonucleotides used for DNA amplification and mutagenesis.

Type	protein	Res#	Mut	Restr	Sequence
forward	Contactin 2	29	N/A	BglII	AATAATAGATCTTTTTCCCAGGGAACCCCAGC
reverse	Contactin 2 (Ig1-6)	608	N/A	NotI	AATAATGCGGCCGCACCTCGGACCAGGACTGTG
reverse	Contactin 2 (fe)	1004	N/A	NotI	AATAATGCGGCCGCTCTCACAATGTGGACTTCGGC
forward	Contactin 2	N/A	F175,178D	N/A	AACGACATCCCAACGGATGGGCGT
reverse	Contactin 2	N/A	F175,178D	N/A	GGGGTCCTCGTTGAGGAGCCAGCG
forward	Contactin 2	N/A	R169D (after F175N)	N/A	TTTGTCCTACGACTGGCTCCTCAACGAGG
reverse	Contactin 2	N/A	R169D	N/A	CCTGGGTAGTGGGCAGGT
forward	Contactin 2	N/A	L210D	N/A	CTACTCTTGCGACGCTACCAGCCACCTGGACTTC
reverse	Contactin 2	N/A	L210D	N/A	TTGCCCAGGTCCGAGGCA
forward	Contactin 2	N/A	L332D	N/A	GCCTGAGTGGGACAAGGTGATCTC
reverse	Contactin 2	N/A	L332D	N/A	TGAGCTTGCACAATGATG
forward	Contactin 2	N/A	A353D	N/A	CTGTGCTGCGGACGGCAAGCCTC
reverse	Contactin 2	N/A	A353D	N/A	CCCCAACGTAAGTTGGAAC
forward	Contactin 2	N/A	R508D	N/A	CCTGTCTGTGGACGATGCAACGAAGATCACGC
reverse	Contactin 2	N/A	R508D	N/A	ATCCCGGTACTGTTGGCT
forward	Contactin 2	N/A	M540D	N/A	TGACCCCACTGACGACCTCACGTTCACCTGG
reverse	Contactin 2	N/A	M540D	N/A	GCGAGGCGTGGCACTGT
forward	Contactin 2	N/A	N78A	N/A	GTGGAAGATGGCCGGCACAGAGATG
reverse	Contactin 2	N/A	N78A	N/A	CTATAGGTGGCTGGAGGG
forward	Contactin 2	N/A	N200A	N/A	CGCCCGCACCGCTGCCTCGGACC
reverse	Contactin 2	N/A	N200A	N/A	ATGTACAGGTTCCCTGTGGTC
forward	Contactin 2	N/A	N500A	N/A	GGGCAAAGCCGCCAGTACCGGGA
reverse	Contactin 2	N/A	N500A	N/A	ATGAAGTTCTCAGCAAAGC
forward	Contactin 1	21	N/A	BamHI	AATAATGGATCCGACTTTACCTGGCACAGAAGATATG
reverse	Contactin 1 (fe)	996	N/A	NotI	AATAATGCGGCCGCGCCTGAAATTTTGACTTGAGACAC

Supplemental references

S1: Chataigner, L.M.P., Gogou, C., den Boer, M.A., Frias, C.P., Thies-Weesie, D.M.E., Granneman, J.C.M., Heck, A.J.R., Meijer, D.H., and Janssen, B.J.C. (2022). Structural insights into the contactin 1 - neurofascin 155 adhesion complex. Nature communications 13, 6607. 10.1038/s41467-022-34302-9.